

Biomechanical response of the human pelvis: a high-rate vertical loading pilot study

A Thesis

Presented to
the faculty of the School of Engineering and Applied Science
University of Virginia

in partial fulfillment
of the requirements for the degree

Master of Science

by

John J. Christopher

May

2016

APPROVAL SHEET

The thesis
is submitted in partial fulfillment of the requirements
for the degree of
Master of Science



AUTHOR

The thesis has been read and approved by the examining committee:

Dr. Jeff Crandall

Advisor

Dr. Richard Kent

Dr. Jason Kerrigan

Accepted for the School of Engineering and Applied Science:



Craig H. Benson, Dean, School of Engineering and Applied Science

May
2016

ABSTRACT

The proliferation of improvised explosive devices (IEDs) in recent military conflicts have caused injuries which present new challenges to the biomechanics community. Vehicle-mounted U.S. and coalition warfighters are being exposed to extreme loading conditions from under-body blasts (UBB), and are suffering devastating injuries. One region of the body that is injured in these UBB events is the pelvis. For UBB events, the primary load vector is applied vertically through the seat, thus loading the pelvis in a direction and at a rate never before researched. This study aims to quantify the mechanical response of the component pelvis from a high-rate vertical load, so as to improve understanding of the pelvic response and to provide data for anthropomorphic test device (ATD) development.

In ten post-mortem human surrogate (PMHS) pelvises, the superior surface of the sacrum was rigidly secured to a 6-axis load cell, which was then rigidly mounted to an effective mass, equivalent to that of a 50th percentile male torso. This assembly was resting against a seat platen, which was impacted by a linear impactor, providing a single high-rate loading condition into the specimen. Accelerometers were used to quantify the boundary conditions. Additionally, accelerometers, an angular rate sensor, and strain gauges were used to capture the response of the pelvis.

The average input seat velocity for this study was 5.9 ± 0.3 m/s with a time to peak of 6.6 ± 0.2 ms. This input condition yielded a calculated axial stiffness of 995 ± 159 kN/m before there was a failure at the rigid potting boundary. The average failure time was 4 ± 0.6 ms, and the peak axial force was -6 ± 1.8 kN. The primary rotation was positive about the y-axis, and the moment at time of failure was 311 ± 16 Nm.

This study offers detailed biomechanical response data of the component pelvis from a single high-rate impulse, including force and moment response corridors, as well as strain response and sacrum acceleration. This data is necessary for the development of a biofidelic pelvis for UBB applications, both for finite element analysis, and ATD development.

Table of Contents

Abstract	i
Thesis Introduction	1
The problem	1
The injured pelvis.....	1
Past pelvis injury characterization	3
Thesis Summary.....	4
Methods.....	5
Test fixture	5
Specimens	7
Specimen positioning and potting.....	8
Instrumentation	10
Calculations.....	12
Experimental results.....	14
Test fixture input.....	14
Injuries	15
Pelvis and sacrum response.....	16
Detailed results for each test	19
Pelvis 001.....	19
Pelvis 002.....	20
Pelvis 003.....	23
Pelvis 004.....	26
Pelvis 005.....	29
Pelvis 006.....	32
Pelvis 007.....	35
Pelvis 008.....	37
Pelvis 009.....	40
Pelvis 010.....	44
Discussion	47
Boundary Conditions	47
Force-response corridors.....	48
Axial force-displacement	49
Pelvis/Sacrum response.....	50
Fractures and stiffness.....	52

Axial and shear moment arms.....	52
Limitations	53
Thesis summary and conclusions.....	53
References.....	55
Appendix A.....	57

TABLE OF FIGURES

Figure 1 - This schematic shows the two primary load paths into a seated occupant during a UBB event..	1
Figure 2 - Male pelvis showing blood supply vessels. Image courtesy of Zygote Body	3
Figure 3 - Schematic of linear impactor/transfer piston, polyurethane pulse shaper, and seat platen.	5
Figure 4 - A detailed schematic showing how the pelvis is situated in the testing rig.	6
Figure 5 - A photograph of a specimen in position on Telemachus ready for a test.....	6
Figure 6 - MADYMO force and acceleration plots.	7
Figure 7 - General pelvis anatomy with local coordinate system defined by Wu.	9
Figure 8 - A detailed schematic showing how the pelvis is positioned in the testing rig with the local pelvis coordinate system.	9
Figure 9 - A schematic showing the ASIS-PS angle.....	10
Figure 10 - Pelvis schematic showing targeting locations for strain gauges and the posterior mount of the acceleration block.	11
Figure 11 - Sagittal x-ray image of a pelvis potted in position.....	11
Figure 12 - Schematic showing moment arms and forces acting on a point.....	13
Figure 13 - Seat acceleration response of all tests.	14
Figure 14 - Acceleration vs. displacement plot up to time of failure.....	14
Figure 15 - Test 004: Sagittal CT image of the pelvis, post-test, at the midline of the sacrum.	16
Figure 16 - Acoustic emission signals plotted with a force trace to determine fracture timing	17
Figure 17 - Sacrum angular rate data about the y-axis.....	18
Figure 18 - Sacrum resultant accelerations.	18
Figure 19 - Sacrum acceleration along the pelvis x-axis	18
Figure 20 - Sacrum acceleration along the pelvis z-axis.....	19
Figure 21 - Injury picture for test 001	19
Figure 22 - Pelvis strains for test 002	20
Figure 23 - Pelvis forces and moments, as well as sacrum angular rate for test 002.....	21
Figure 24 - Sacrum accelerations and angular rate, and pelvis moment about the y-axis for test 002	21
Figure 25 - Seat and carriage accelerations for test 002.	22
Figure 26 - Seat and carriage displacements for test 002.....	22
Figure 27 - Injury picture for test 002.....	22
Figure 28 - Pelvis strains for test 003	23
Figure 29 - Pelvis forces and moments, as well as sacrum angular rate for test 003.....	24
Figure 30 - Sacrum accelerations and angular rate, and pelvis moment about the y-axis for test 003	24
Figure 31 - Seat and carriage accelerations for test 003.	25

Figure 32 - Seat and carriage displacements for test 003.....	25
Figure 33 - Injury picture for test 003.....	26
Figure 34 - Pelvis strains for test 004	26
Figure 35 - Pelvis forces and moments, as well as sacrum angular rate for test 004.....	27
Figure 36 - Sacrum accelerations and angular rate, and pelvis moment about the y-axis for test 004	27
Figure 37 - Seat and carriage accelerations for test 004.	28
Figure 38 - Seat and carriage displacements for test 004.....	28
Figure 39 - Injury picture for test 004.....	29
Figure 40 - Pelvis strains for test 005	29
Figure 41 - Pelvis forces and moments, as well as sacrum angular rate for test 005.....	30
Figure 42 - Sacrum accelerations and angular rate, and pelvis moment about the y-axis for test 005	30
Figure 43 - Seat and carriage accelerations for test 005	31
Figure 44 - Seat and carriage displacements for test 005.....	31
Figure 45 - Injury picture for test 005.....	32
Figure 46 - Pelvis strains for test 006.	32
Figure 47 - Pelvis forces and moments, as well as sacrum angular rate for test 006.....	33
Figure 48 - Sacrum accelerations and angular rate, and pelvis moment about the y-axis for test 006	33
Figure 49 - Seat and carriage accelerations for test 006.	34
Figure 50 - Seat and carriage displacements for test 006.....	34
Figure 51 - Injury picture for test 006.....	35
Figure 52 - Pelvis strains for test 007	35
Figure 53 - Pelvis Fx and Fz for test 007.....	36
Figure 54 - Seat and carriage accelerations for test 007.	36
Figure 55 - Seat and carriage displacements for test 007.....	37
Figure 56 - Injury picture for test 007.....	37
Figure 57 - Pelvis strains for test 008.	38
Figure 58 - Pelvis forces and moments, as well as sacrum angular rate for test 008.....	38
Figure 59 - Sacrum accelerations and angular rate, and pelvis moment about the y-axis for test 008	39
Figure 60 - Seat and carriage accelerations for test 008.	39
Figure 61 - Seat and carriage displacements for test 008.....	40
Figure 62 - Injury picture for test 008.....	40
Figure 63 - Pelvis strains for test 009	41
Figure 64 - Pelvis forces and moments, as well as sacrum angular rate for test 009.....	42
Figure 65 - Sacrum accelerations and angular rate, and pelvis moment about the y-axis for test 009	42

Figure 66 - Seat and carriage accelerations for test 009	43
Figure 67 - Seat and carriage displacements for test 009.....	43
Figure 68 - Injury picture for test 009.....	44
Figure 69 - Pelvis strains for test 010	45
Figure 70 - Pelvis forces and moments, as well as sacrum angular rate for test 010.....	45
Figure 71 - Sacrum accelerations and angular rate, and pelvis moment about the y-axis for test 010	46
Figure 72 - Seat and carriage accelerations for test 010	46
Figure 73 - Seat and carriage displacements for test 010.....	47
Figure 74 - Injury picture for test 010.....	47
Figure 75 - Response corridor of Fz forces.....	48
Figure 76 - Response corridor of My moments	49
Figure 77 - Axial force-displacement plots up to fracture	50
Figure 78 - Schematic of the pelvis being loaded by the seat.....	51
Figure 79 - Schematic of the pelvis indicating the areas of high compressive strain adjacent to the SI joints.....	51
Figure 80 - Schematic of the axial and shear forces experienced by the pelvis, as well as the positive moment about the y-axis.....	52
Figure A-1: Strain gauge data from the ‘A’ gauges for test 002.....	57
Figure A-2: Strain gauge data from the ‘C’ gauges for test 002.....	57
Figure A-3: Strain gauge data from the ‘A’ gauges for test 003.....	58
Figure A-4: Strain gauge data from the ‘C’ gauges for test 003.....	58
Figure A-5: Strain gauge data from the ‘A’ gauges for test 004.....	59
Figure A-6: Strain gauge data from the ‘C’ gauges for test 004.....	59
Figure A-7: Strain gauge data from the ‘A’ gauges for test 005.....	60
Figure A-8: Strain gauge data from the ‘C’ gauges for test 005.....	60
Figure A-9: Strain gauge data from the ‘A’ gauges for test 006.....	61
Figure A-10: Strain gauge data from the ‘C’ gauges for test 006.....	61
Figure A-11: Strain gauge data from the ‘A’ gauges for test 007.....	62
Figure A-12: Strain gauge data from the ‘C’ gauges for test 007.....	62
Figure A-13: Strain gauge data from the ‘A’ gauges for test 008.....	63
Figure A-14: Strain gauge data from the ‘C’ gauges for test 008.....	63
Figure A-15: Strain gauge data from the ‘A’ gauges for test 009.....	64
Figure A-16: Strain gauge data from the ‘C’ gauges for test 009.....	64
Figure A-17: Strain gauge data from the ‘A’ gauges for test 010.....	65

Figure A-18: Strain gauge data from the 'C' gauges for test 010..... 65

TABLE OF TABLES

Table 1 - Percentage of casualties with specific fractures	2
Table 2 - Summary of previous pelvis studies.....	4
Table 3 – Summary of specimen demographics	8
Table 4 – Test matrix showing component mass, pelvis angle, and input acceleration.	12
Table 5 – Rotations about the y-axis to transform from the load cell to the pelvis coordinate system	12
Table 6 - Summary of dx measurements	13
Table 7 – Peak seat velocities integrated from seat accelerations.	15
Table 8 – Failure time, axial and shear force at failure, and moment about the y-axis at failure.	17
Table 9 – Summary of calculated axial stiffness values.	50
Table 10 – Distal pelvis fractures categorized to show two primary load paths	51

THESIS INTRODUCTION

The problem

Since the onset of Operation Iraqi Freedom (OIF) in 2003 and Operation Enduring Freedom (OEF) in 2001, U.S. military forces have been engaged in a new style of warfare. The widespread use of improvised explosive devices (IEDs) against ground forces has changed modern combat tactics and has introduced new challenges to frontline soldiers, medical doctors, and researchers. Efforts have been made to protect vehicle-mounted seated soldiers against under-body blast (UBB) events through the use of mine resistant vehicles, but without understanding the threshold of injuries at these loading rates, future designs cannot be effectively implemented (Belmont, Jr. 2010).

Due to the high likelihood that lower extremities would be injured in a UBB event, initial research studies focused their investigations on that body region's response (Ramasamy 2011). Additionally, new mechanisms of lower extremity injuries, such as brisance effect fractures, led researchers to focus their efforts on understanding the mechanism of such injuries, and establishing prevention and treatment techniques (Ramasamy 2011; Bailey 2013). While the initial research focus was on the lower extremities, the second primary load path into a seated soldier is through the pelvis (Figure 1).

Since pelvic fractures can pose a high risk of death due to subsequent blood loss from severed arteries, it is important to understand the response in order to better protected from injury. Quantifying the response of the pelvis will not only yield the response of the pelvis itself, but the output loads from the pelvis can serve as input loads to the regions immediately superior to it, like the lumbar and thoracic spine. The dynamic response of vertebral bodies has been of concern due to the percentage of injuries sustained along the different spinal sections, such as studied by Stemper et al. in 2012. Having a realistic input condition will help such efforts.

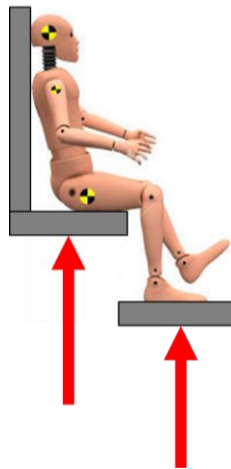


Figure 1 - This schematic shows the two primary load paths into a seated occupant during a UBB event.

The injured pelvis

From October 2001 thru August 2009, American combat forces sustained over 40,000 casualties in OIF and OEF combined (Belmont, Jr. 2010). Many of these injuries resulted from IEDs and a significant portion affected the lower extremities and pelvis. Through January 2005, an estimated 54% of the soldiers injured had sustained a musculoskeletal injury to the extremities (pelvis excluded) (Belmont, Jr. 2010). In a report published by Alvarez et al., underbody blast events in 456 wounded in action (WIA) cases and 152 killed in action (KIA) cases were analyzed

for types of injury (Alvarez 2011). A summary of the percentage of casualties with specific fractures is listed in Table 1. Although the pelvis is only amongst 5% of the casualties in WIA cases, it is injured in nearly half of the KIA cases. Some types of pelvic injuries from theater include Tile's type B and C fractures due to vertical shear of the pelvis and are mostly involved with disrupted sacroiliac joints (Bailey 2011). Coccyx and ischial tuberosity fractures occurred as well.

Table 1 - Percentage of casualties with specific fractures. (Alvarez 2011).

Body Region	KIA	WIA
Head	51%	4%
Neck (hyoid)	17%	<1%
Face	39%	8%
Hand	9%	2%
Upper Extremity	44%	10%
Cervical Spine	18%	5%
Thoracic Spine	21%	12%
Lumbar Spine	26%	18%
Ribs/Sternum	54%	5%
Pelvis	46%	5%
Femur	33%	7%
Tibia/Fibula	32%	18%
Foot/Ankle	32%	26%

There have been several studies investigating lower extremity injuries, both from automotive and UBB loading conditions¹, but there seems to be a lack of understanding in the literature about the response of the pelvis from axial loads. Since current anthropomorphic test devices (ATDs) are not designed for axial loading, their injury prediction abilities are lacking. Measuring failure tolerances and calculating a stiffness value of the component pelvis will be useful data towards the development of a more biofidelic pelvis.

The risk of severe hemorrhage and hypovolemic shock exists due to the high concentration of large arteries (Figure 2), but any injury to the pelvis decreases mobility, which can hinder the immediate escape from a threat as well as long-term recovery. In addition to uncontrolled hemorrhage, other serious complications are possible, including infection and sepsis. Infection and septic shock can arise when a fractured pelvis introduces a sharp bony edge to a thin-walled gastrointestinal organ. Abdominal infection will increase morbidity and prolong recovery time for a soldier wounded in action.

¹ Crandall et al. 1998; Yoganandan et al. 1997; Funk et al. 2002; Wang et al. 2001; Ramasamy et al. 2010; Schueler et al. 1995; McKay & Bir 2009.

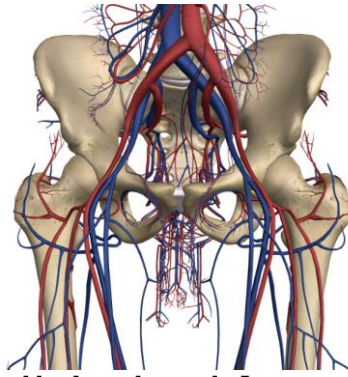


Figure 2 - Male pelvis showing blood supply vessels. Image courtesy of Zygote Body.

Past pelvis injury characterization

In the 1990s, there was a growing concern for injuries sustained in automotive side impact collisions. A considerable amount of pelvic research was conducted to better understand how a pelvis responds in these types of collisions and to identify injury thresholds². All of these studies focused on either frontal or lateral loading conditions. Guillemot et al. reported that the average maximum force imparted on a pelvis when loaded to failure through the acetabulum is 1750 N (Guillemot 1998). These tests were conducted at quasi-static rates and ‘pseudo-stiffness’ values were calculated based on the force-displacement response.

In 2006, Salzar et al. conducted experiments focused on quantifying injury tolerance of the hip (Salzar 2006). The study reported that fracture initiation force recorded by the axial femur load cell varied with femur position. The minimum fracture force occurred at a force of 2260 ± 660 N when the femurs were in an extended abduction position. When the femurs were in an extended neutral position, the maximum fracture force was recorded at 5820 N.

In a separate study conducted by Salzar et al. in 2009, the lateral load path through the pelvis was compared in both quasi-static and dynamic loading conditions (Salzar 2009). This study found that both impact location (acetabulum or iliac wing) and load rate affect the lateral load distribution through the bony pelvis. They concluded that for high-rate acetabulum loading, the combined load at fracture was 2800 ± 860 N, and for high-rate iliac wing loading, the combined force at fracture was 3020 ± 1050 N (Salzar 2009).

A summary of previous study conclusions in Table 2 suggests a wide range of fracture forces. These fracture forces are applicable to varying frontal or lateral loading environments. The current study will investigate axial loading and compare results to fracture forces and stiffness values reported in Table 2.

Although these previous studies focused on automotive frontal and lateral loading, it is important to note that the pelvis has been axially loaded before, but not studied in detail. Whole body ejection seat studies, performed by Salzar, axially loaded the body faster than the automotive studies, but were not focused on component pelvis response (Salzar et al. 2009). Additionally, the loading pulse is much longer during an ejection seat impulse compared to an underbody blast from an IED, and the typical injuries are thoracic spinal injuries, not the pelvis (Lewis 2006).

² Guillemot et al. 1995; Guillemot et al. 1997; Guillemot et al. 1998; Bouquet et al. 1998

Table 2 - Summary of previous pelvis studies

Study	Direction	Static Fracture Force	Dynamic Fracture Force	Pelvis Stiffness
Cesari 1982	Lateral	~1800 N	~10 kN impact force	
Chamouard 1993	Lateral	~7000 N	-	Static stiffness: 35 kN/m Dynamic stiffness: 300 kN/m Damping coefficient: 1800 N-s/m
Guillemot 1998	Lateral	1100 – 3450 N	~4 kN input force	Acetabulum: 201-423 N/mm Iliac wing: 46-211 N/mm
Salzar 2009	Lateral	-	Acetabulum loaded: 2800 ± 860 N Iliac Wing loaded: 3020 ± 1050 N	-
Salzar 2006	Frontal	-	Extended abduction: 2260 ± 660 N Extended, neutral: 5820 N	-

Thesis Summary

The primary focus of this research thesis was to investigate the failure tolerance of the component pelvis subjected to a high-rate vertical loading event, and calculate the axial stiffness.

The research was conducted at the University of Virginia's Center for Applied Biomechanics with the support of fellow graduate students and support staff.

The results of this research will offer a detailed analysis of the response of the pelvis from the prescribed input condition and can be used to develop more biofidelic ATDs as well as refine finite element computer models.

METHODS

Test fixture

A test rig, Telemachus, was designed and built to simulate a high-rate vertical load delivered to a component pelvis. The Telemachus component test rig was inspired by Odyssey, U.Va.'s whole body under-body blast simulator (Bailey 2013). The system is a horizontal system and is powered by a free standing pneumatic linear impactor. Figure 3-Figure 5 detail the test rig and how the pelvis is situated on the rig. It was designed to have rigid boundaries on the superior and inferior sides of the test specimen that were instrumented with laboratory accelerometers to measure inputs. The 20 kg seat is not rigidly coupled with the pelvis and is constrained to move along a single axis. Similarly for the response, the carriage is restricted to be able to only translate along the same axis. Because of the constrained motion of the rig, it is assumed that the primary loading vector acts only along the same axis and the influence of out of plane loading vectors is minimal. Different seat impulses can be obtained by varying the launch pressure of the pneumatic impactor, as well as by varying the geometry and/or type of polyurethane layer.

The mass of the carriage that the load cell is secured to is an integral part of the design. The recruited mass of the torso/upper body is important when considering testing configurations of the component pelvis. The reaction mass that the pelvis should react against after being impacted should be equivalent to the effective mass of the upper body and applied at the sacrum. In order to estimate the effective mass, a lumped-mass human body model (MADYMO, TASS International) was utilized.

Three acceleration pulses were prescribed to the MADYMO 50% male human model. Each pulse was an idealized triangular pulse with a rise time to peak of 3 ms. The three varying acceleration peaks were 200 g, 300 g, and 400 g. Initial contact between the seated male and the rigid seat was prescribed and 1g of acceleration was applied.

The response of the model was taken at the L5/sacrum joint above the pelvis. The resulting peak force (z-axis) and acceleration at the time of peak were used to calculate the effective mass and guide construction of the carriage. The resulting effective mass on test fixture was approximately 12 kg. Figure 6 shows the force and acceleration plots from the MADYMO model.

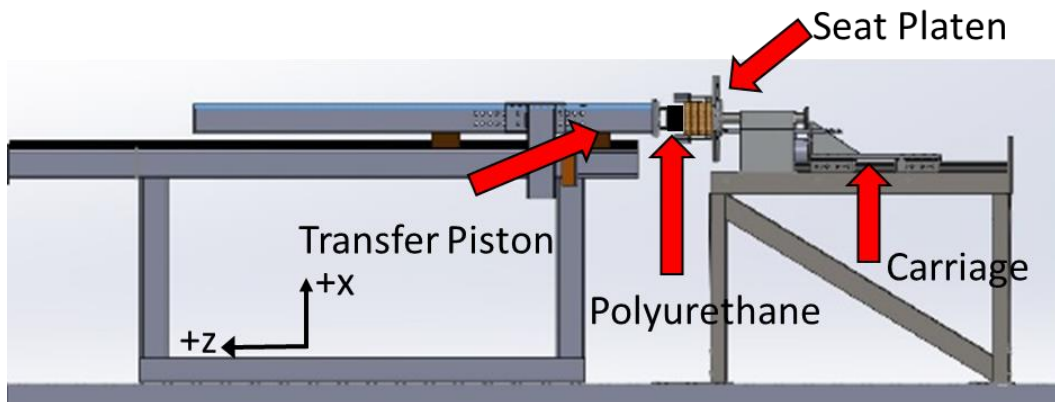


Figure 3 – Schematic of linear impactor/transfer piston, polyurethane pulse shaper, and seat platen.

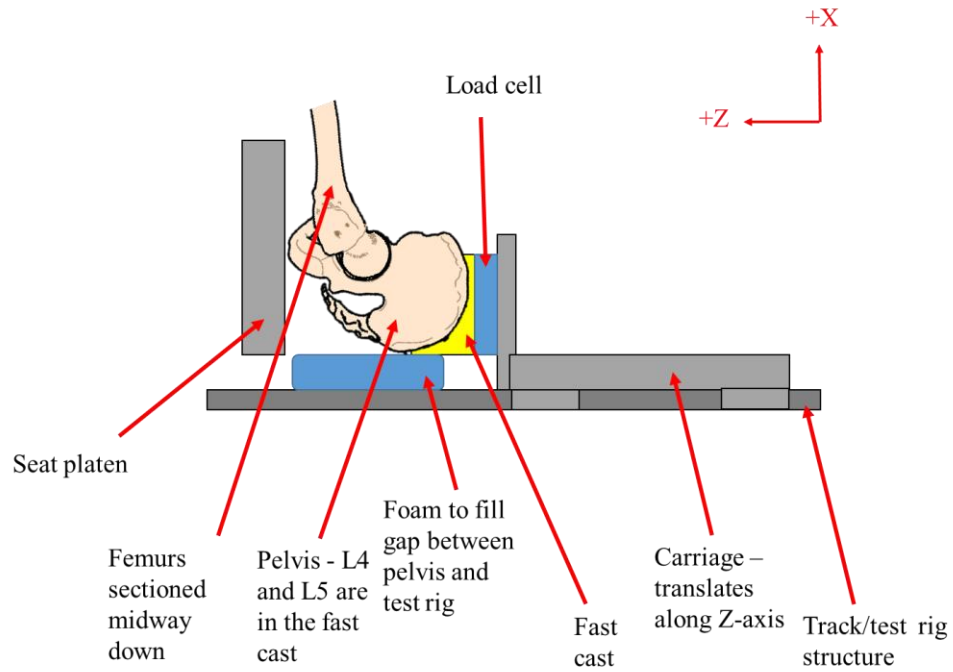


Figure 4 - A detailed schematic showing how the pelvis is situated in the testing rig.

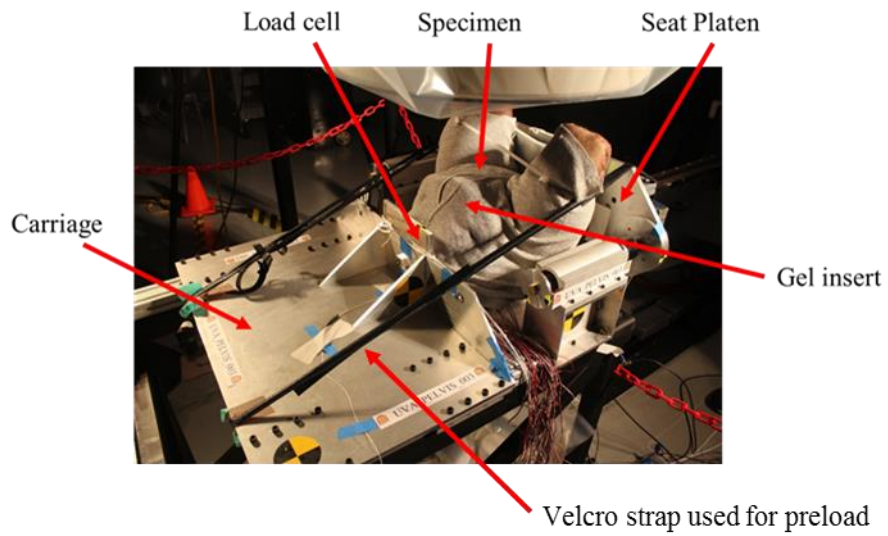


Figure 5 – A photograph of a specimen in position on Telemachus ready for a test. Various components are pointed out with arrows.

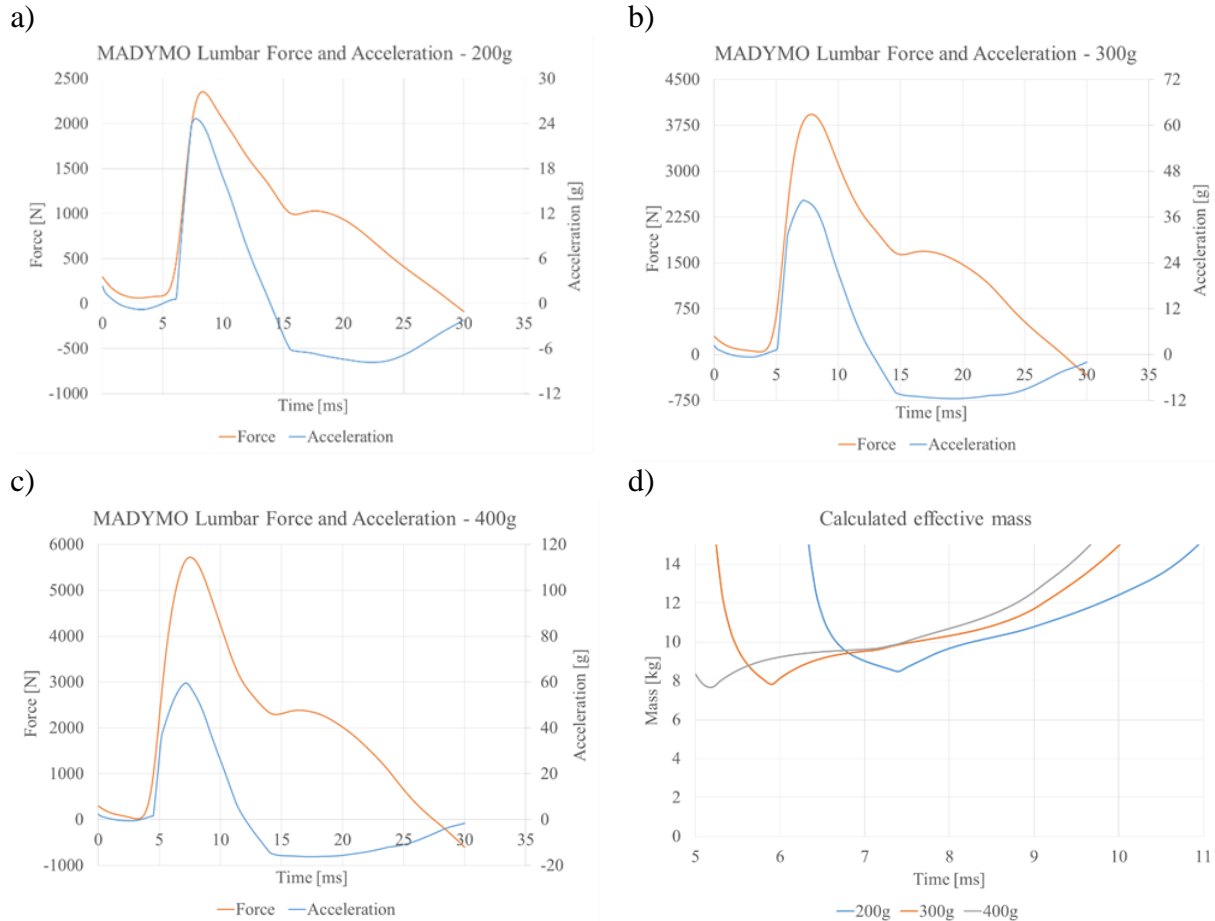


Figure 6 – a-c) MADYMO force and acceleration plots for 200, 300, and 400g input accelerations. d) Calculated effective mass plots. The final effective mass on Telemachus had a mass of 12 kg.

Once potted, the specimen was rigidly secured to a load cell on the carriage. Before testing, a preload was applied using Velcro straps to compress the pelvis (Figure 5). The preload was calculated based on the mass of the torso and how much force it would generate when subjected to gravity. An assumed mass of 35 kg was used to determine the pre-load for each pelvis to be ~350 N (Clauser 1969).

Specimens

Ten fresh, unembalmed post mortem human surrogates (PMHS) were obtained for testing through tissue suppliers accredited by the American Association of Tissue Banks. The test protocols were subject to review by the University of Virginia Institutional Review Board for Human Surrogates. A summary of their anthropometry is shown in Table 3. Each specimen was sectioned from the level of L4 to mid-femur. Only male subjects were selected for this study to minimize potential geometric effects on force response. The mean age of the specimens was 52 ± 11 years, the mean weight was 80.3 ± 14.4 kg, and mean height was 172.4 ± 13.6 cm.

The femurs have been shown to load the bony pelvis in both lateral and frontal motor vehicle collisions and are suspected as a load path in axial loading of the seated pelvis (Salzar 2006). In order to represent realistic loading conditions into the pelvis, the femurs with surrounding soft tissue were left intact and included to the level of the mid-thigh. Inter-

abdominal organs were removed, weighed and properly stored. The average mass of tissue removed was approximately 3 kg. This mass was later replaced with a gelatin mixture of equal mass.

Table 3 – Summary of specimen demographics

Test #	Specimen #	Sex	Age	Height (cm)	Weight (kg)	BMD T-score	COD
001	502	M	70	136	45.5	-2.9	Aneurysm
002	570	M	59	175	83	-1.1	Heat Stroke
003	571	M	58	175	83.4	-1.7	Cardiac Arrest
004	591	M	44	177	86	-0.9	Bacterial Pneumonia
005	581	M	52	178	78.5	0.6	Heart Attack
006	594	M	36	185	103.9	0.5	Leukemia
007	595	M	42	170	77	-2.2	Anoxic Brain Injury
008	603	M	40	180	80.3	-0.2	Suicide
009	602	M	61	168	79	-0.5	Stroke
010	609	M	58	180	86.2	-1.2	Malignant brain neoplasm
Average			52	172.4	80.3	-1	
Std. dev.			11	13.7	14.4	1.1	

Specimen Positioning and Potting

The SAE coordinate system was selected as the coordinate system for the boundary condition measurements and to define the ‘global’ coordinate system (Society of Automotive Engineers 1995). The local coordinate system of the pelvis is defined by a plane using anatomical landmarks, similar to the method by Wu in 2002. The four landmarks in Figure 7 that define the plane are the left and right anterior-superior iliac spines (ASIS), and the left and right posterior-superior iliac spines (PSIS). The midpoint of the vector between the left and right PSIS is what the accelerations of this study were transformed to. The x-axis is then defined as the vector between the midpoint of the left and right PSIS and the midpoint of the left and right ASIS. The y-axis is the vector normal to the x-axis and parallel to the vector connecting the left and right PSIS. The cross product of the x- and y-axes defines the z-axis, which is positive towards the inferior pelvis. Figure 8 shows a schematic of the pelvis in position on Telemachus and the orientation of the local pelvis coordinate system. The notation for the global coordinate system is X, Y, and Z, while the notation for the local pelvis coordinate system is x, y, and z. Z is the axis that the seat and carriage move along, and X is perpendicular to Z and parallel to gravity. Y is defined by the cross product of the two axes, and is parallel to the surface of the seat.

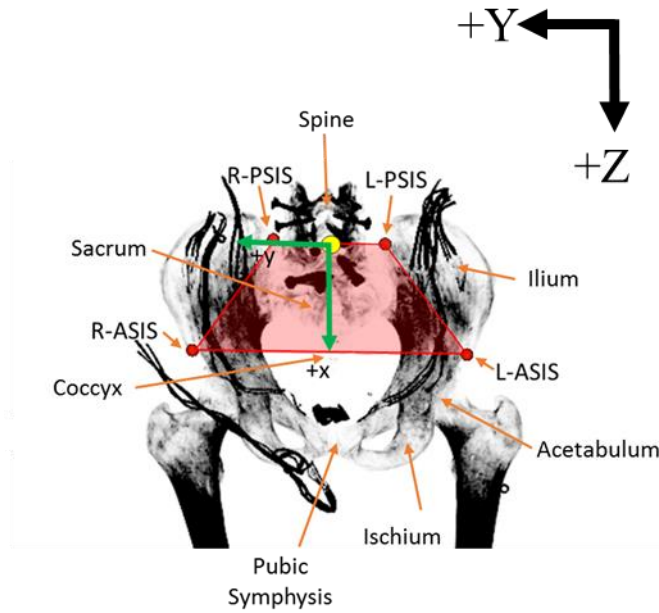


Figure 7 – General pelvis anatomy with local coordinate system defined by Wu. Specimens for this study were sectioned from L4 to mid-femur.

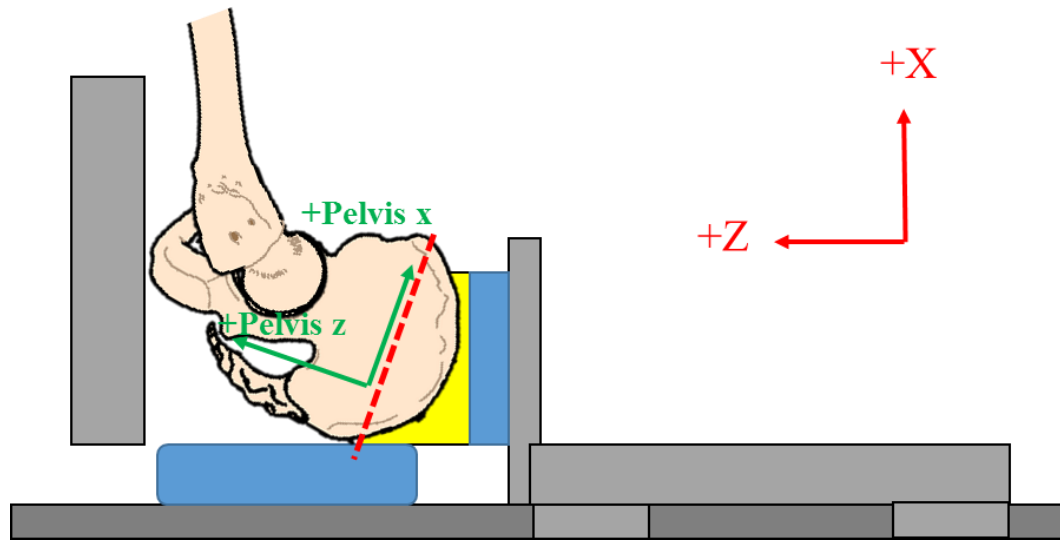


Figure 8 - A detailed schematic showing how the pelvis is positioned in the testing rig with the local pelvis coordinate system.

Soft tissue was removed from the L4 and L5 vertebral bodies to accommodate a potting box, and three screws were carefully inserted to ensure that the load was shunted through the disc. These screws were inserted into the L5 vertebral body midway between the superior and inferior surfaces on the anterior side. They were driven down until they engaged the S1 sacral body. Shorter screws were partially driven into L4 for added rigidity when the FastCast was poured. Additionally, care was taken to preserve soft tissues that contribute strength to the pelvis. Specifically, the anterior and posterior sacroiliac joint ligaments were left intact, as well as the bilateral sacrotuberous ligaments. Muscles and other connective tissues were preserved as much as possible in the pelvic ring and only removed at locations of instrumentation. The

fibrocartilage of the pubic symphysis and its connective ligaments were also preserved in order to help maintain the integrity of the pelvic ring.

Before the spine was fixed in the FastCast (Goldenwest Manufacturing, Grass Valley, CA) potting medium, the pelvis had to be angled into a seated posture. Bony landmarks, specifically the left and right anterior-superior iliac spines and the pubic symphysis, were used to position the pelvis in a seated posture. The angle between the plane formed by the three bony landmarks and the global Z-axis is called the ASIS-PS angle and is only used for positioning/potting the pelvis. Figure 9 is a schematic showing the ASIS-PS angle from the lateral view.

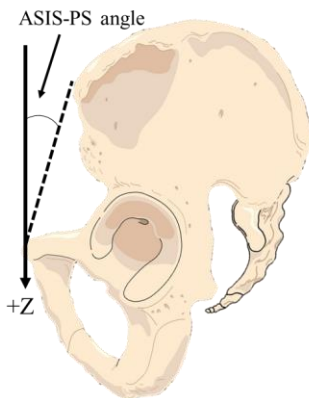


Figure 9 – A schematic showing the ASIS-PS angle. The ASIS-PS angle is defined as the angle between the plane defined by the anterior superior iliac spines and the pubic symphysis, and the Z-axis. Neutral is defined as an angle of 0, and a negative angle indicates a posterior tilt.

The first two specimens were potted and tested at a -45° ASIS-PS angle (posterior tilt). The overall physical look and impact location of the seat with the sacrum did not seem reasonable for a usual upright sitting posture. Therefore, a second literature review was conducted after the first two tests to better identify a normal sitting posture.

Dankaerts et al. studied the difference in sacral angles at S2 between patients sitting in a ‘usual’ sitting posture on a rigid, horizontal seat and sitting in a ‘slumped’ posture (Dankaerts 2006). From Dankaerts’ results and using CT analysis combined with bony measurements on the Global Human Body Model Consortium finite element model (GHBMC; <http://www.ghbmc.com/>), it was determined that the usual sitting posture would correlate to an ASIS-PS angle of $-22 \pm 13^\circ$ (posterior tilt). The remainder of the pelvis were potted according to the angle related to Dankaerts’ study.

Instrumentation

The ten component tests were instrumented to capture the boundary conditions as well as the specimen’s response. A four-degree of freedom sensor cube was rigidly secured to the posterior pelvis at the S1/S2 level. The cube measured local x-, y-, and z- accelerations as well as angular rates about the y-axis. CT measurements were used to transform the cube data to the local pelvis coordinate system. The instrumentation to capture the boundary conditions included a 7270A accelerometer (Endevco Meggitt Sensing Systems, Irvine, CA) on the seat platen, and a 7264B accelerometer (Endevco Meggitt Sensing Systems, Irvine, CA) on the carriage, along with a 6-axis steering column load cell mounted on the carriage to record the force response at the sacrum. Additionally, acoustic emission sensors, attached next to the SI joints on the ilium,

were used for tests 2 thru 10 for fracture detection and a host of strain elements were used throughout the pelvis (Figure 10). The majority of the strain gauges were tri-axial rosettes. Once each specimen was fully instrumented, a pre-test CT scan was ordered to be able to precisely measure instrument location before testing. Figure 11 shows a sagittal x-ray image of a pelvis potted in position with the sacrum acceleration block in view.

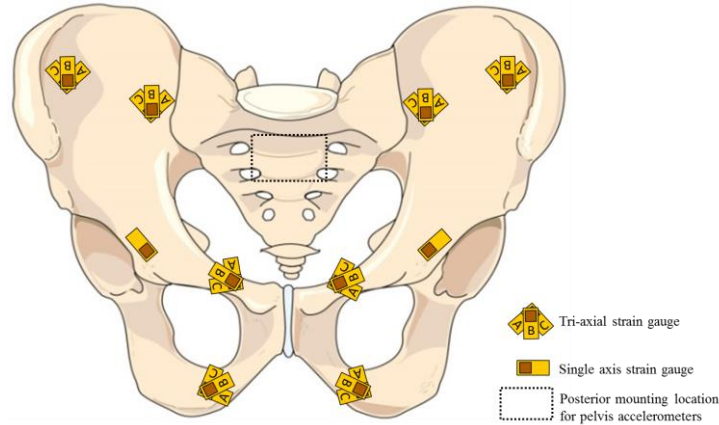


Figure 10 - Pelvis schematic showing targeting locations for strain gauges and the posterior mount of the acceleration block.

Data was collected using a DTS SlicePro data acquisition system (Diversified Technical Systems, Seal Beach, CA) as well as a Hi-Techniques Synergy data acquisition system (Hi-Techniques, Inc., Madison, WI). Channels were sampled at a rate of 1MHz. All acceleration data were filtered with a 4-pole Butterworth filter set to 1650 Hz (CFC1000). All other data were filtered with a 4-pole Butterworth filter set to 20 kHz.

Each specimen was tested once with a target input acceleration of 150g and a time to peak of 3ms, which is similar to tests conducted by Bailey (Bailey 2015). Table 4 is the test matrix including the component mass. After each test, injuries were evaluated through post-test CT scans and dissection by a trained medical examiner.

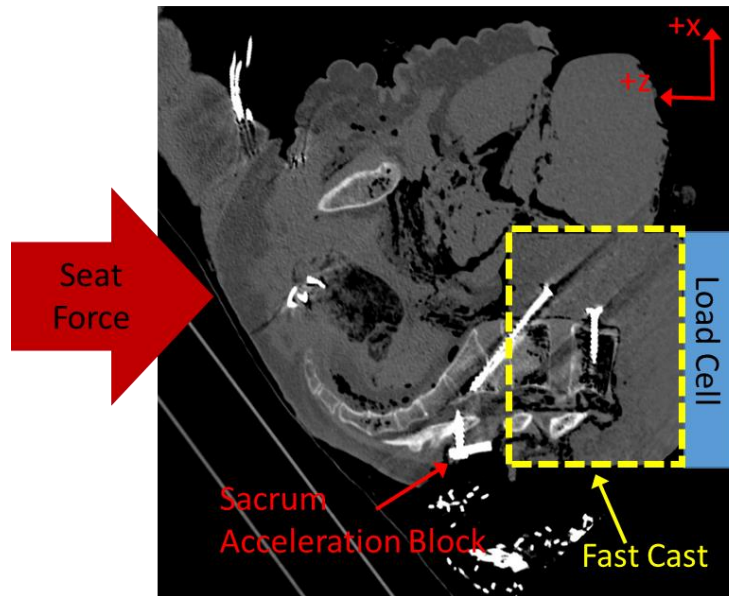


Figure 11 -- Sagittal x-ray image of a pelvis potted in position with the sacrum acceleration block in view.

Table 4 – Test matrix showing component mass, pelvis angle, and input acceleration.

Test #	Component mass (kg)	Pelvis Angle (degrees)	Target input acceleration (g)	Target time to peak acceleration (ms)
001	16.4	-45	150	3
002	-			
003	23.1	-22		
004	21.1			
005	25.1			
006	25.2			
007	21.5			
008	24.5			
009	23.3			
010	18.6			
Average	22.1			
Std. Dev.	3.0			

Calculations

The forces and moments recorded by the load cell were transformed to the origin of the pelvis coordinate system, defined as the midpoint of the vector between the left and right PSIS. It was assumed that the FastCast was a rigid body in order to perform the translation. The load cell's X- and Z-axes were then rotated with a standard rotation matrix (Eq. 1) to be in line with the pelvis coordinate system. The rotations were minimal, no more than 15 degrees for tests 3-10. The rotations were more for tests 1 and 2 because of the initial angle they were potted in. The specific values, measured from CT images, to rotate forces from a global measurement to the pelvis coordinate system are summarized in Table 5. The rotations were about the y-axis.

$$[F_{x_{pelvis}} \quad F_{z_{pelvis}}] = [F_{X_{translated}} \quad F_{Z_{translated}}] \begin{bmatrix} \cos\theta & -\sin\theta \\ \sin\theta & \cos\theta \end{bmatrix} \quad (\text{Eq. 1})$$

Table 5 –Rotations about the y-axis to transform from the load cell to the pelvis coordinate system.

Test #	Angle from global to local (degrees)
001	32
002	23
003	6.5
004	14.5
005	7
006	13
007	8
008	9
009	9.5
010	11.5

CT data was used to measure the distance, dZ , between the center of the pelvis coordinate system (simply represented by the blue circle in Figure 12) and the inferior most portion of the pelvis to be impacted by the seat. This measurement was used along with M_y , F_x , and F_z to calculate the moment arm, dX , of the axial force (F_z) as shown in Equation 2. Table 6 summarizes the moment arm values, both before and after being corrected for the coordinate system rotation.

The strain gauge data were examined to determine fracture time, but the acoustic sensors proved to be a better indicator. The strain gauges were used, however, to show how the pelvis was responding during the loading phase and to help account for anomalies in the force data, such as load shifting.

$$dX = \frac{My - (Fx * dZ)}{Fz} \quad (\text{Eq. 2})$$

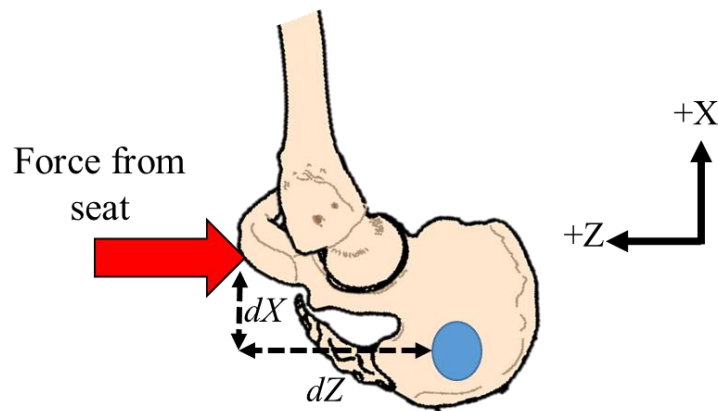


Figure 12 – Schematic showing moment arms and forces acting on a point.

Table 6 - Summary of dX measurements and the corrected values based on the small rotations of the pelvis coordinate system. Test 001 was omitted because failure timing was not detected, and 007 was omitted because M_y was not captured.

Test #	dX in cm. (measured from CT)	dX corrected for rotation of pelvis coordinate system (cm)
002	6	5.5
003	3.6	3.5
004	9.1	8.8
005	6	6
006	3.2	3.1
008	3.9	3.9
009	1.7	1.7
010	2.4	2.4

CT data was used to determine the corners of the surfaces of the accelerometer block and of the bony landmarks used to define the pelvis coordinate system. These measurements were used to define the sacrum block axes and transform them to the pelvis coordinate system through

translation and rotation. Since the sacrum block only had four channels, it was assumed that the rotations about the x- and z-axes were minimal when performing the sacrum acceleration transformations. Once transformed, the accelerations were used to calculate the resultant pelvis acceleration and show how the pelvis moved along the x- and z-axes.

The axial force and moment about the y-axis are used to calculate response corridors using the methodology outlined by Lessley 2004. Axial force-displacement corridors were also calculated using the pelvis Fz force, and from doubly integrated acceleration data from the seat and carriage. The resulting slopes of the force-displacement plots yielded an axial stiffness value.

EXPERIMENTAL RESULTS

Test fixture input

Telemachus proved to be very repeatable as shown by the seat acceleration traces in Figure 13. Figure 14 shows acceleration of the seat versus displacement. The consistency amongst all the tests shows that the input was not affected by the pelvis that it was impacting. Table 7 shows that this acceleration was equivalent to an average seat velocity of 5.9 ± 0.3 m/s in 6.6 ± 0.2 ms.

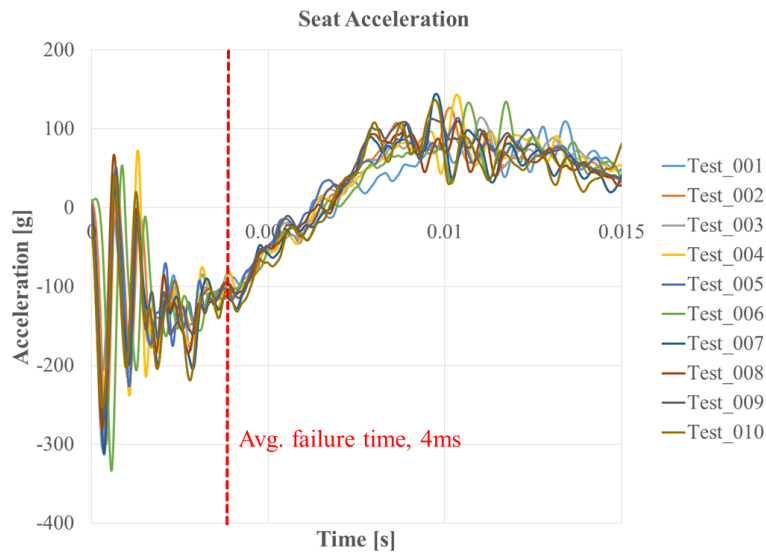


Figure 13 – Seat acceleration response of all tests. Telemachus proved to be very repeatable. Sharp peaks with short duration at the beginning of the trace were not included in the 150 g in 3 ms assessment. The sharp spikes in the acceleration data can be attributed to the seat platen flexing upon impact from the transfer piston.

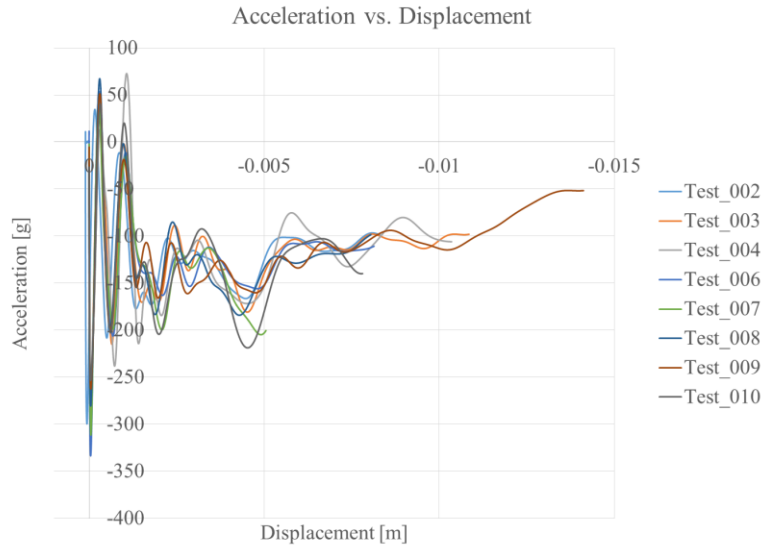


Figure 14 – Acceleration vs. displacement plot up to time of failure. Test 005 was omitted from this plot due to excessive acceleration ringing. The consistent acceleration from test to test shows that the input was not affected by the pelvis.

Table 7 – Peak seat velocities integrated from seat accelerations.

Test #	Peak Seat Velocity (m/s)	Time to peak (ms)
UVA_PELVIS_001	-5.3	6.9
UVA_PELVIS_002	-5.8	6.5
UVA_PELVIS_003	-5.8	6.4
UVA_PELVIS_004	-6.0	6.3
UVA_PELVIS_005	-5.7	6.2
UVA_PELVIS_006	-5.9	6.6
UVA_PELVIS_007	-6.3	6.8
UVA_PELVIS_008	-5.9	6.8
UVA_PELVIS_009	-5.9	6.5
UVA_PELVIS_010	-6.5	6.7
average	-5.9	6.6
standard deviation	0.3	0.2

Injuries

Each specimen sustained a sacrum injury near the interface with the FastCast and screws used for potting. The majority of the injuries did not destroy the integrity of the pelvic ring; however, there was one test where there was a complete disruption of the posterior arch of the pelvic ring. The pubic symphysis remained intact for all tests, and there were no full disruptions

of the sacroiliac joints. Injury descriptions and images are listed below for each test. A representative CT image of a sacral fracture is shown in Figure 15.

The majority of the injuries were located on the sacrum or at the potting interface. The fractures around the pot are artifactual due to the rigid boundary and not characteristic of injuries seen in theater. The distal sacrum/coccyx injuries are likely not artifactual, but rather were caused by the high-rate loading from the seat platen.

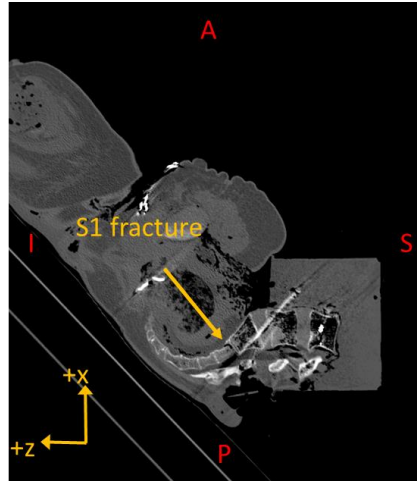


Figure 15 - Test 004: Sagittal CT image of the pelvis, post-test, at the midline of the sacrum. Also in view are the potted L4 and L5 vertebral bodies. The yellow arrow indicates the fracture that was sustained during testing. This image is oriented to show the sacrum in a testing position even though the imaging was done in a hospital CT machine. The hip is extended because of how the specimen is positioned for scanning.

Pelvis and Sacrum Response

In the plots below, F_x is the pelvis force along the x-axis. F_y and F_z are the pelvis forces along the y- and z-axis, respectively. A_x is the sacrum acceleration along the pelvis x-axis. A_y and A_z are the sacrum accelerations along the pelvis y- and z-axis, respectively. The angular rate sensor measured sacrum rotations about the pelvis y-axis, and M_y is the pelvis moment about the y-axis. The seat and carriage acceleration and displacements are measured along the global Z-axis.

Since all of the specimens fractured at the potting interface, only data up to time of fracture is reported. Time of fracture was determined for nine of the ten tests using the acoustic emission sensors in a similar manner as previous studies conducted by Salzar and Funk (Salzar 2006; Funk 2002). When the acoustic data recorded an amplified, near instantaneous response, the time corresponding to the initiation of the response was considered the failure time. Test one did not have acoustic sensors employed. Figure 16 depicts acoustic signals plotted with lumbar F_z to determine fracture time and force at failure. Table 8 summarizes times of failure, as well as axial forces and moments about the y-axis at the fracture time. The average axial force when the potting failed for tests 2-10 was -5949 ± 1777 N and the average moment about the y-axis at fracture was 311 ± 157 Nm. The average shear force was -1845 ± 825 N. The average failure time was 4 ± 0.6 ms.

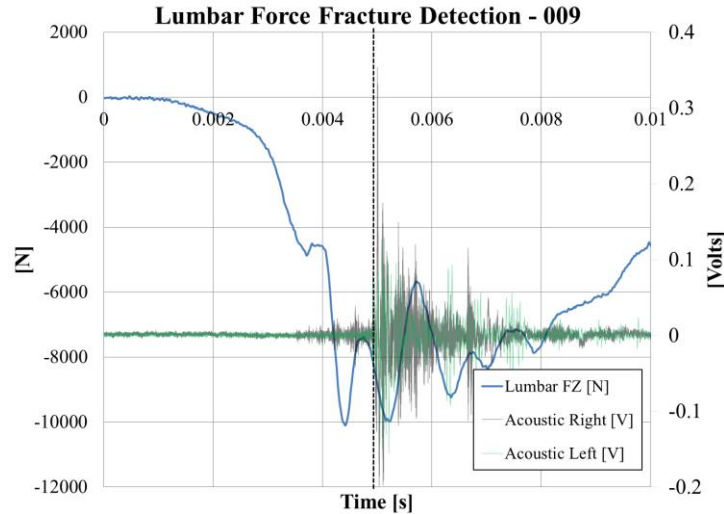


Figure 16 – Acoustic emission signals plotted with a force trace to determine fracture timing and force at fracture. The dotted line indicates the point at which the acoustic signal significantly increases (greater than 1 order of magnitude of the base signal), indicating there was a fracture.

Table 8 – Summary of failure time, axial and shear force at failure, and moment about the y-axis at failure.

Test #	Failure Time (ms)	Fx at Potting Failure (N)	Fz at Potting Failure (N)	My at Potting Failure (Nm)
UVA_PELVIS_001	-	-	-	-
UVA_PELVIS_002	3.9	-2549	-3872	269
UVA_PELVIS_003	4.3	-922	-8167	302
UVA_PELVIS_004	4.2	-3327	-6353	627
UVA_PELVIS_005	4.6	-1950	-7809	496
UVA_PELVIS_006	3.9	-2197	-6590	239
UVA_PELVIS_007	2.9	-351	-2540	-
UVA_PELVIS_008	3.7	-1851	-5873	256
UVA_PELVIS_009	4.9	-2038	-7563	159
UVA_PELVIS_010	3.6	-1422	-4842	137
average	4.0	-1845	-5949	311
standard deviation	0.6	825	1777	157

Sacrum angular rate about the y-axis is plotted in Figure 17. Angular rates at fracture range from about 250-1400 deg/s. The positive trend in the kinematics is in agreement with the positive moments about the y-axis.

Resultant sacrum acceleration is plotted in Figure 18. The two primary accelerations of the resultant are the x- and z-accelerations (Figure 19 & Figure 20). The x-accelerations all follow a negative trend, while the z-accelerations start with a negative trend and then turn positive.

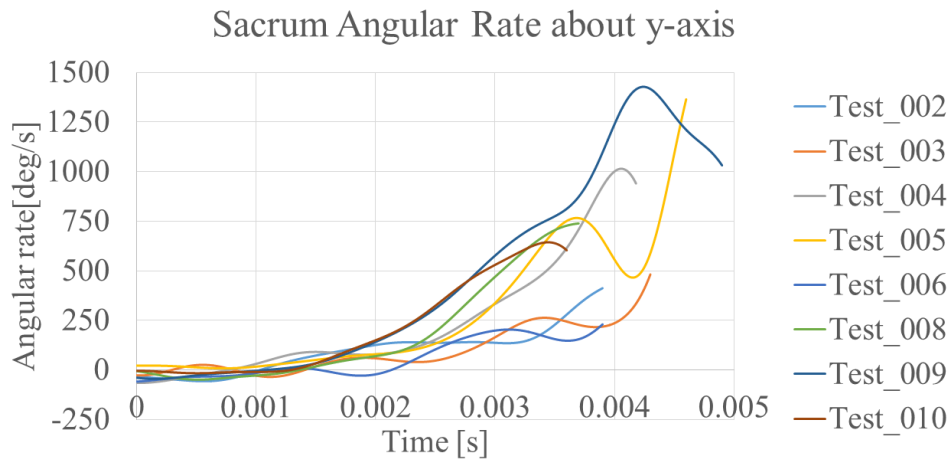


Figure 17 – Sacrum angular rate data about the y-axis. All tests exhibited a positive rotation about the y-axis.

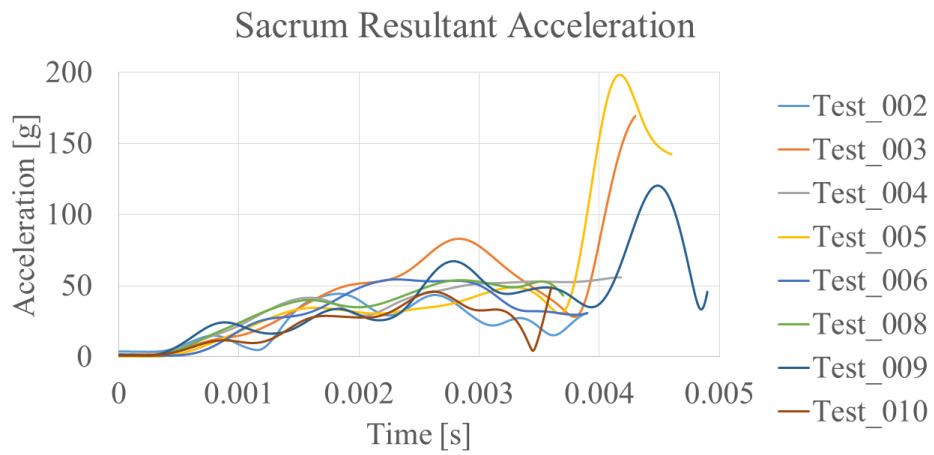


Figure 18 - Sacrum resultant accelerations.

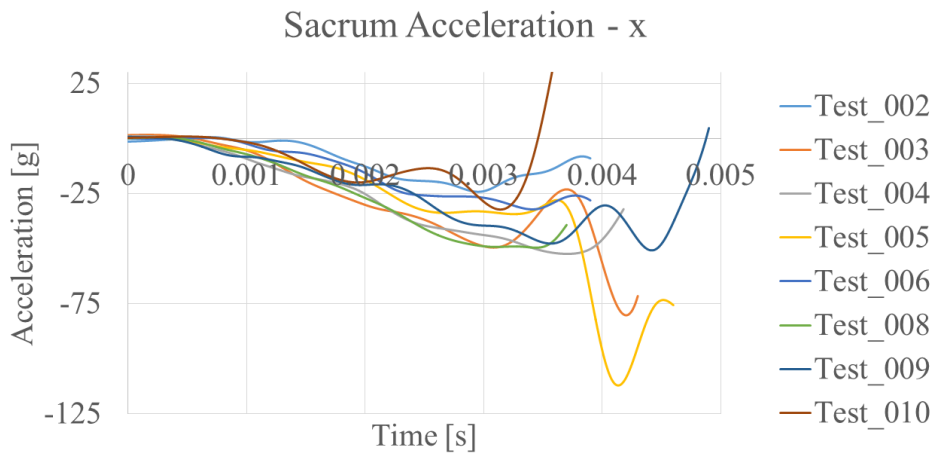


Figure 19 - Sacrum acceleration along the pelvis x-axis. All tests followed a similar negative trend.

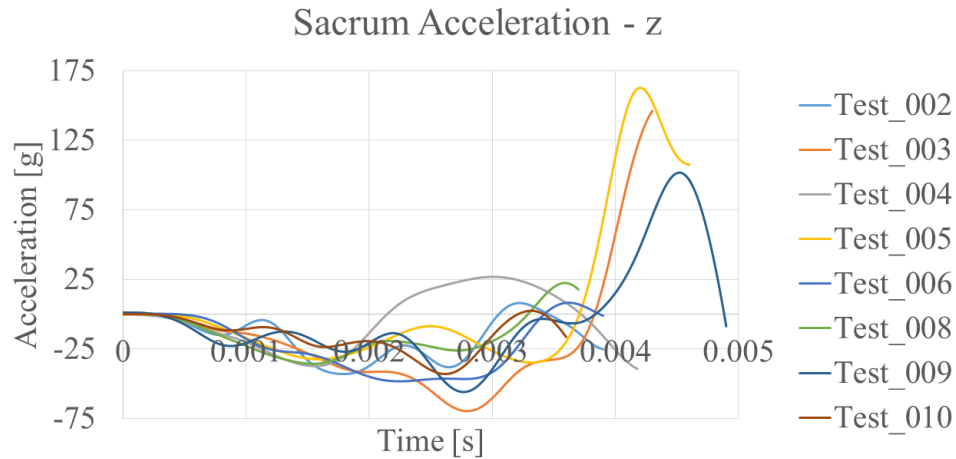


Figure 20 - Sacrum acceleration along the pelvis z-axis. All tests followed a negative and then positive trend.

Detailed results for each test

Below are detailed plots of all sensor data recorded. Since rosette strain gauges were used throughout the pelvis, it should be noted that only the 'B' gauges are plotted below since they were the gauges used for alignment when applying to the bone. Gauges 'A' and 'C' appear in Appendix B.

Pelvis 001

Since Pelvis 001 did not have any acoustic sensors, fracture timing could not be determined.

Notes from the post-test dissection:

Non-displaced, linear fracture with small comminuted bony fragment was noted extending laterally through the entire sacrum at the level of the most cephalad sacral foramen. Figure 21 shows a picture from the dissection of a fracture.



Figure 21 - Injury picture for test 001. Non-displaced, linear fracture with small comminuted bony fragment was noted extending laterally through the entire sacrum at the level of the most cephalad sacral foramen.

Pelvis 002

Figure 22 shows the strain in the pelvis up to failure. The data indicate that the pelvis underwent compression bilaterally at the SI joints, as well as on the ilium (denoted as ‘wings’ in the plots). The left inferior pubis, left acetabulum, and left superior pubis all measured tension. The right acetabulum measured tension and then went into compression, while the right inferior and superior pubis gauges started in compression and then went into tension.

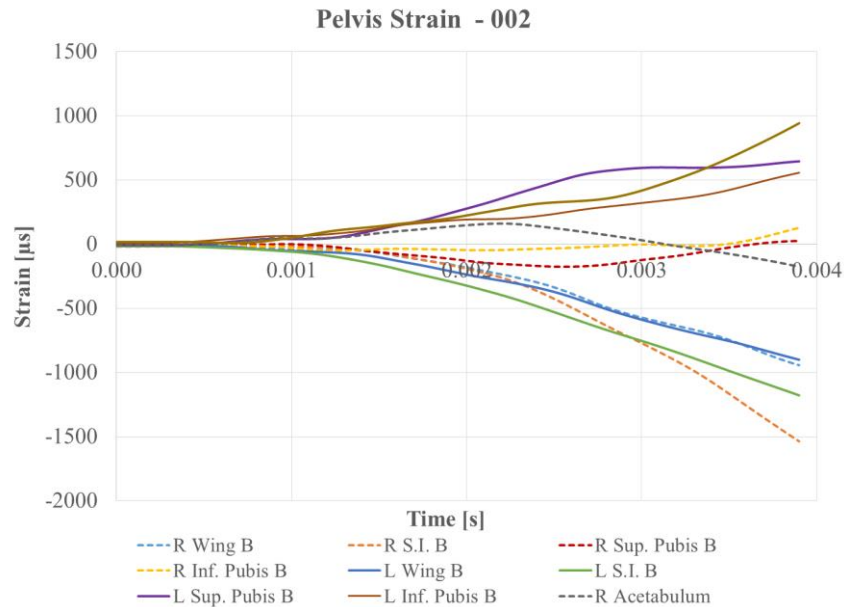


Figure 22 – Pelvis strains for test 002. The left and right S.I. gauges experienced the largest compressive strains.

Figure 23 shows the pelvis forces and moment about the y-axis with strain data as gray dotted lines. Additionally, the angular rate data from the sacrum is plotted. While the primary force was F_z , there was also a significant shear response in F_x . M_y and the angular rate sensor both had a positive trend. F_y experienced a low force response indicating that the off-axis loading was minimal. This is also confirmed in Figure 24 with the sacrum A_y acceleration. The two dominant accelerations were along the z- and x-axes, and both had a predominantly negative response but then trended toward a positive slope at about 3ms.

Figure 25 and Figure 26 show the comparison between the seat and carriage accelerations, as well as the differences in overall displacements. The total distance that the seat moved before failure, as indicated by the acoustic sensor, was about 8.5 mm.

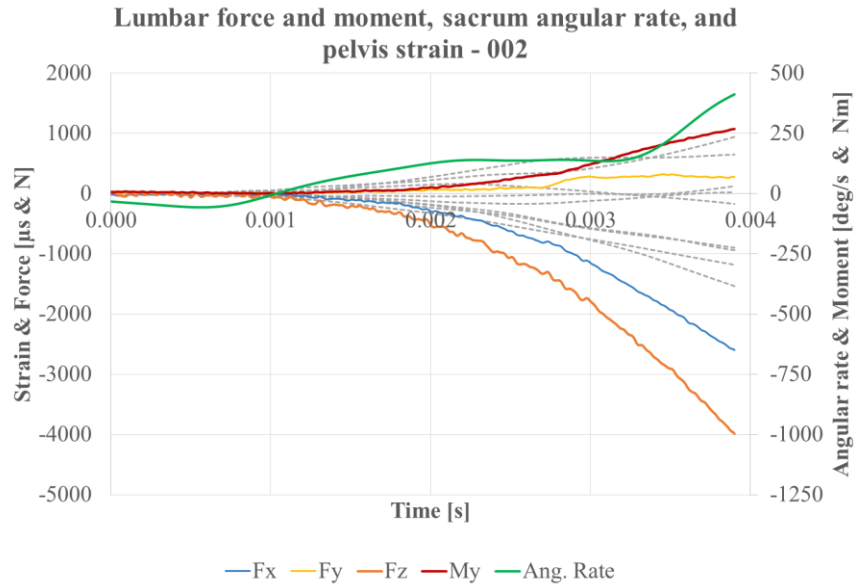


Figure 23 — Pelvis forces and moments, as well as sacrum angular rate for test 002. The gray dotted lines are the strains from the previous figure. Fz was the dominant force. My and the angular rate sensor both had positive trends.

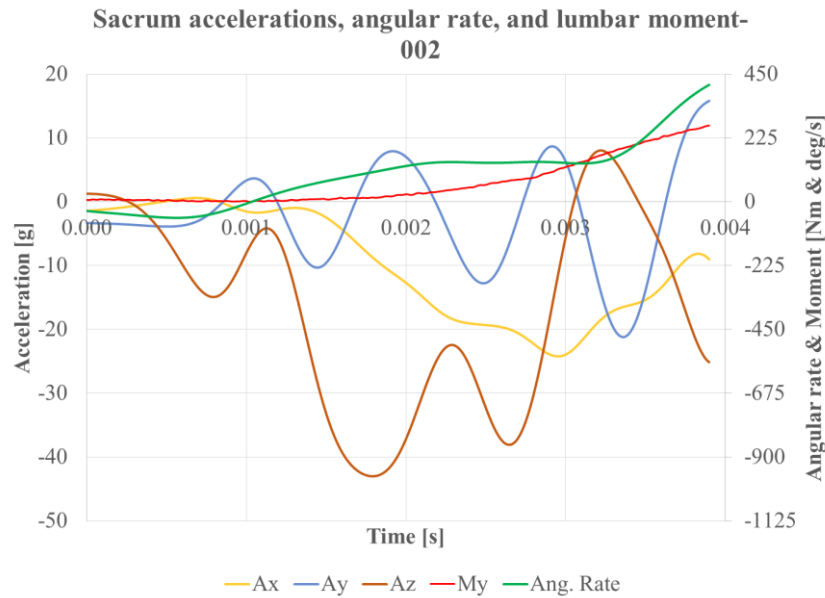


Figure 24 – Sacrum accelerations, angular rate, and pelvis moment about the y-axis for test 002. The two dominant accelerations are along the z- and x-axes and both have a predominantly negative response but then trend with a positive slope at about 3ms.

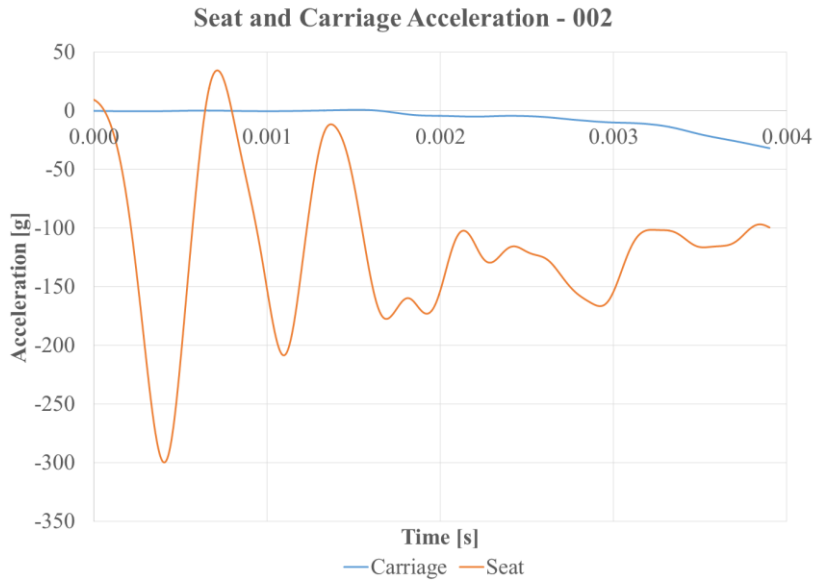


Figure 25 – Seat and carriage accelerations for test 002. The carriage does not start to accelerate until ~1.75ms.

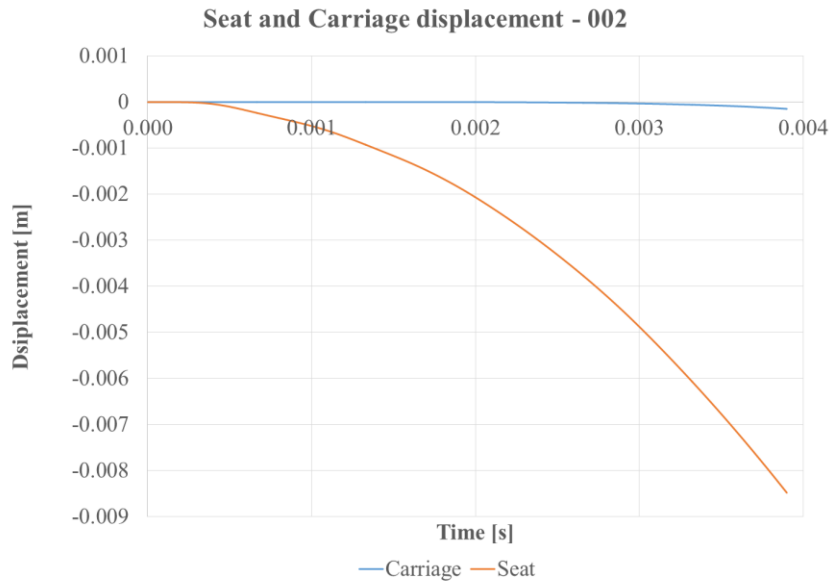


Figure 26 – Seat and carriage displacements for test 002. The displacements were calculated from double integrating the seat and carriage accelerometers. The total seat displacement was ~8.5mm.

Notes from post-test dissection:

Mobile fragment ~5mm at the most inferior portion of the ischium on the left and right. An 8cm fracture was noted extending from the coccyx to the level of S3 on the left lateral sacrum.

Coccyx was noted to have a comminuted fracture. Figure 27 shows a picture from the dissection of a fracture.

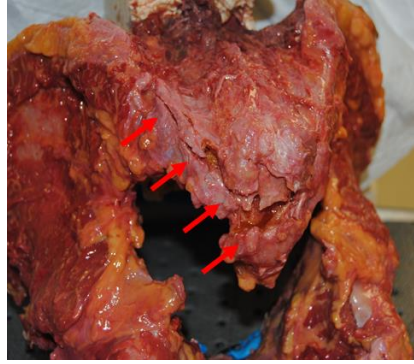


Figure 27 - Injury picture for test 002. An 8cm fracture was noted extending from the coccyx to the level of S3 on the left lateral sacrum.

Pelvis 003

Figure 28 shows the strain in the pelvis up to failure. The left inferior pubis gauge failed and yielded no usable data. The left and right SI gauges both underwent similar compressive loading. Similarly, the left acetabulum and left wing both experienced similar compressive strain. The right inferior pubis gauge was put into tension and peaked before failure.

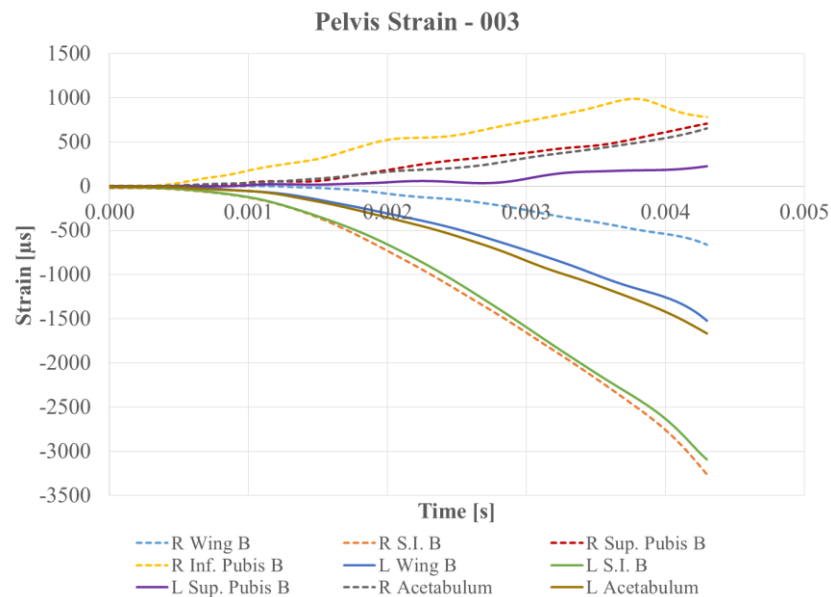


Figure 28 - Pelvis strains for test 003. The left and right S.I. gauges experienced the largest compressive strains.

Figure 29 shows the strain data as gray dotted lines with the pelvis forces and moment about the y-axis plotted in color. Fz was the dominant force, but there was a small shear contribution of about 1 kN along Fx and very little lateral loading along Fy. My and the angular rate sensor both followed a positive trend. In Figure 30, the dominant Az acceleration, as well as the angular rate, have a steep positive rise up to a peak just after 4 ms, which corresponds to the peak in the Fz load. Given the nature of the fractures, these data suggest that the fractures could have been initiating just after 4 ms (in line with the peaks), followed by catastrophic failure at the end of the trace. The positive Az accelerations can be attributed to sacrum rotation about the fixed superior end despite the loading from the seat along the negative z-axis.

Figure 31 and Figure 32 show the comparison between the seat and carriage accelerations, and the differences in overall displacements. The total distance that the seat moved before failure, as indicated by the acoustic sensor, was about 11 mm.

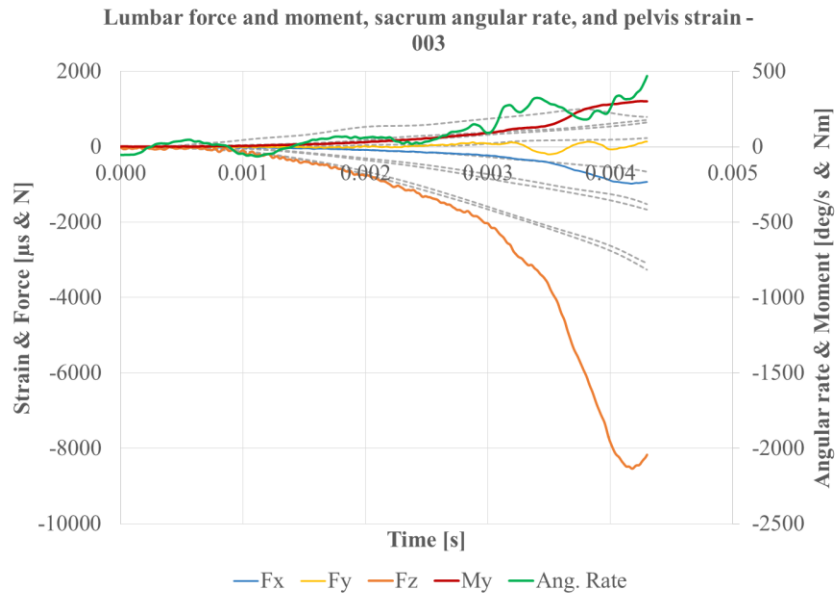


Figure 29 - Pelvis forces and moments, as well as sacrum angular rate for test 003. The dominant Az acceleration has a steep positive rise up to a peak just after 4 ms. The time corresponds to the peak in Fz load.

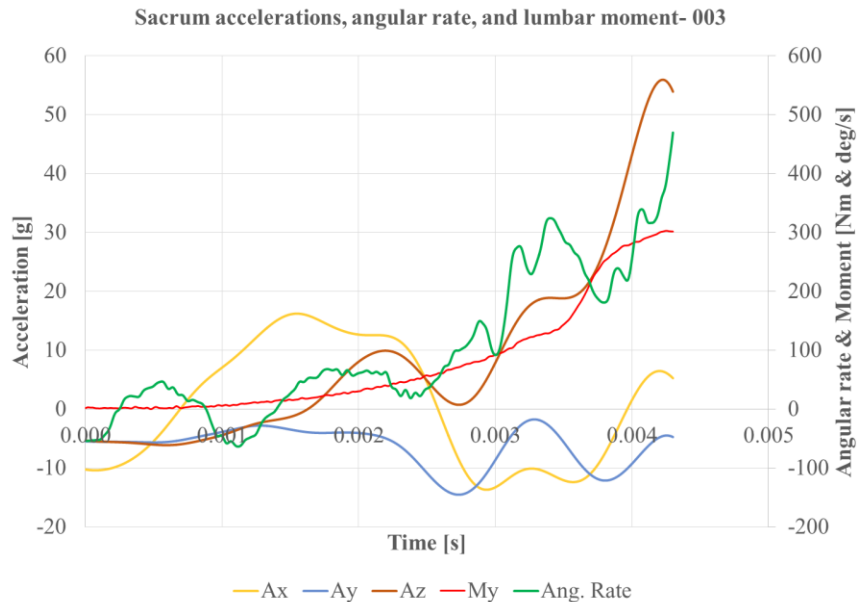


Figure 30 - Sacrum accelerations and angular rate, and pelvis moment about the y-axis for test 003. The dominant Az acceleration has a steep positive rise up to a peak just after 4 ms. The time corresponds to the peak in Fz load.

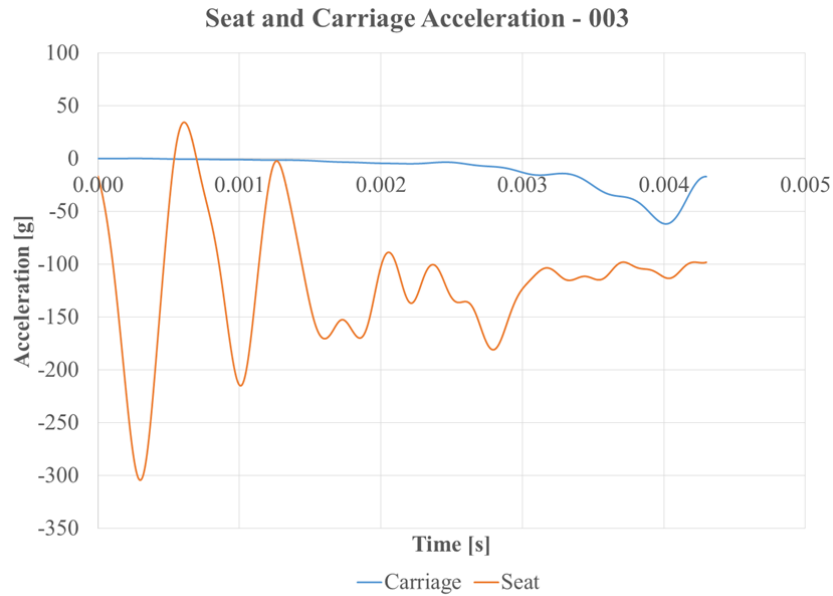


Figure 31 - Seat and carriage accelerations for test 003. The carriage does not start to accelerate until ~2ms.

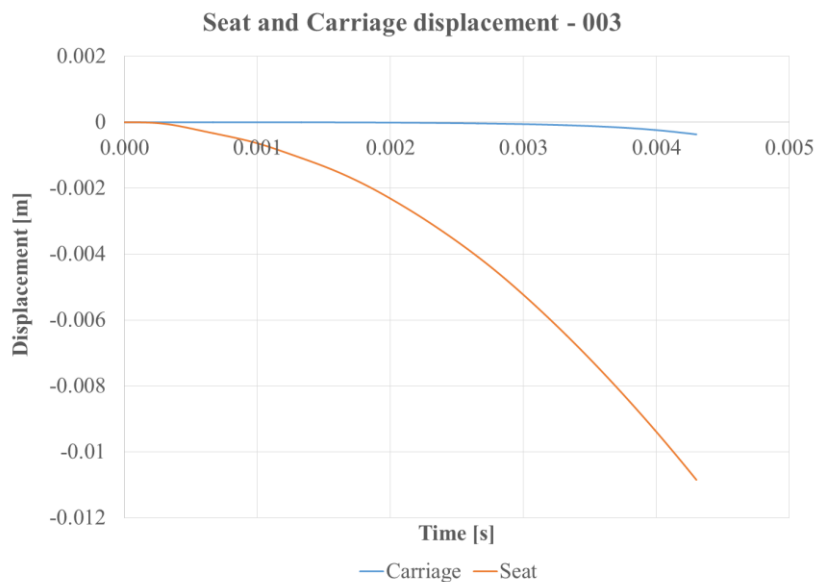


Figure 32 - Seat and carriage displacements for test 003. The displacements were calculated from double integrating the seat and carriage accelerometers. The total seat displacement was ~11mm.

Notes from post-test dissection:

Transverse fracture of the medial sacrum ~1cm below the superior aspect of the sacrum. Fracture continued to the S1 foramen bilaterally then between the S1 foramen. This produced a large mobile fragment of the superior medial portion of the sacrum. Comminuted fracture of the coccyx. Figure 33 shows a picture from the dissection of a fracture.

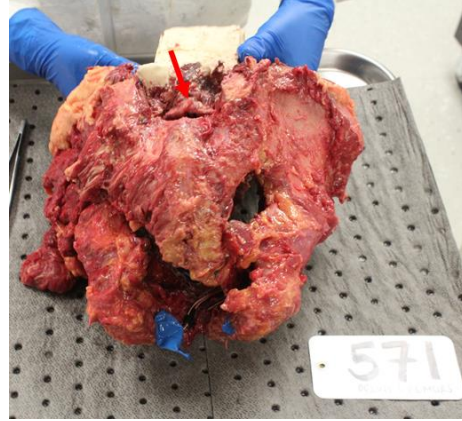


Figure 33 – Injury picture for test 003. Transverse fracture of the medial sacrum ~1cm below the superior aspect of the sacrum.

Pelvis 004

Figure 34 shows the strain in the pelvis up to failure. The left and right SI gauges both underwent similar compressive loading. Similarly, the left wing and right acetabulum both experienced similar compressive strain. The left acetabulum underwent tensile loading while the left superior and inferior pubis gauges experienced a compressive load.

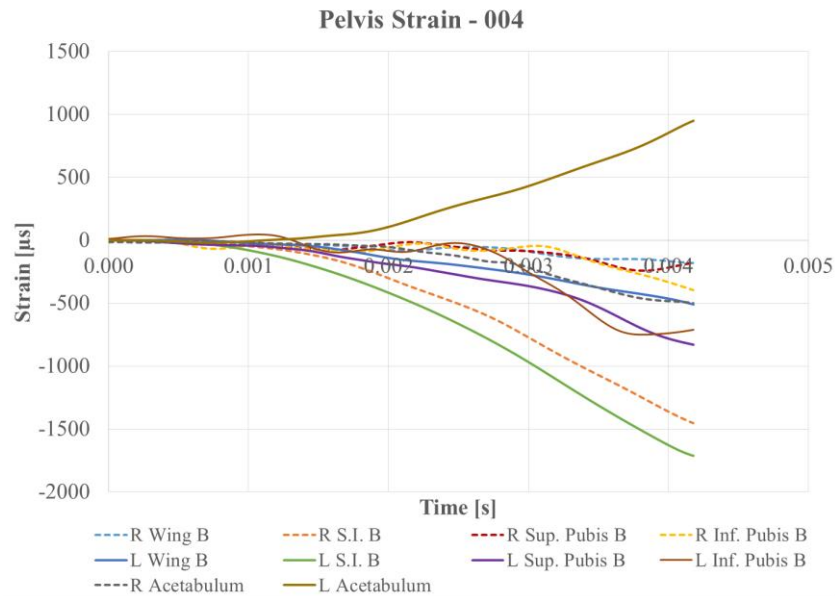


Figure 34 - Pelvis strains for test 004. The left and right S.I. gauges experienced the largest compressive strains.

Figure 35 shows the strain data as gray dotted lines with the pelvis forces and moment about the y-axis plotted in color. Fz was the dominant force, but there was a significant shear response along Fx. Lateral loading along Fy was minimal. Both the angular rate sensor and My experienced positive trends, but only the angular rate sensor reached a peak before failure.

Figure 36 shows the negative and then positive acceleration response recorded by Az. Ax experienced acceleration in the negative direction and reached a minimum just before the angular rate sensor reached its peak. A minimal response from Ay suggested that there was minimal lateral loading.

Figure 37 and Figure 38 show the comparison between the seat and carriage accelerations, as well as the differences in overall displacements. The total distance that the seat moved before failure, as indicated by the acoustic sensor, was about 10 mm, but the carriage had moved about 3 mm by the same time.

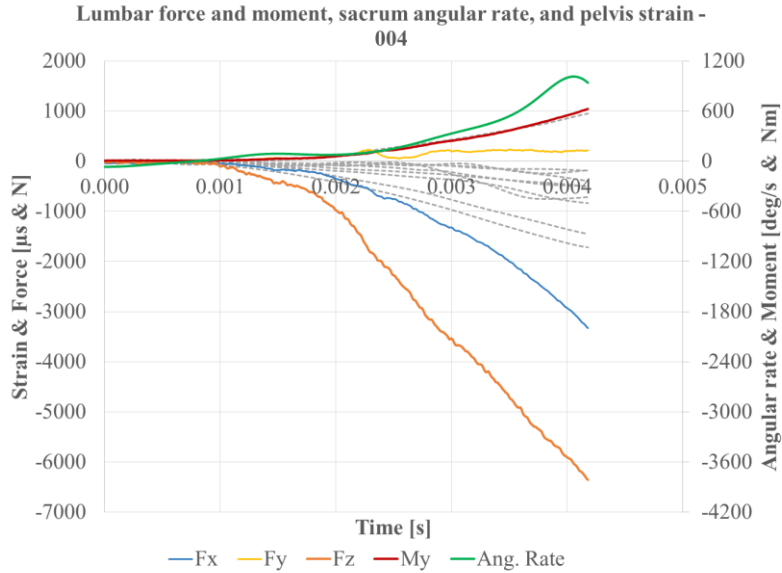


Figure 35 - Pelvis forces and moments, as well as sacrum angular rate for test 004. The gray dotted lines are the strains from the previous figure. Fz was the dominant force, and My and the angular rate sensor both had positive trends.

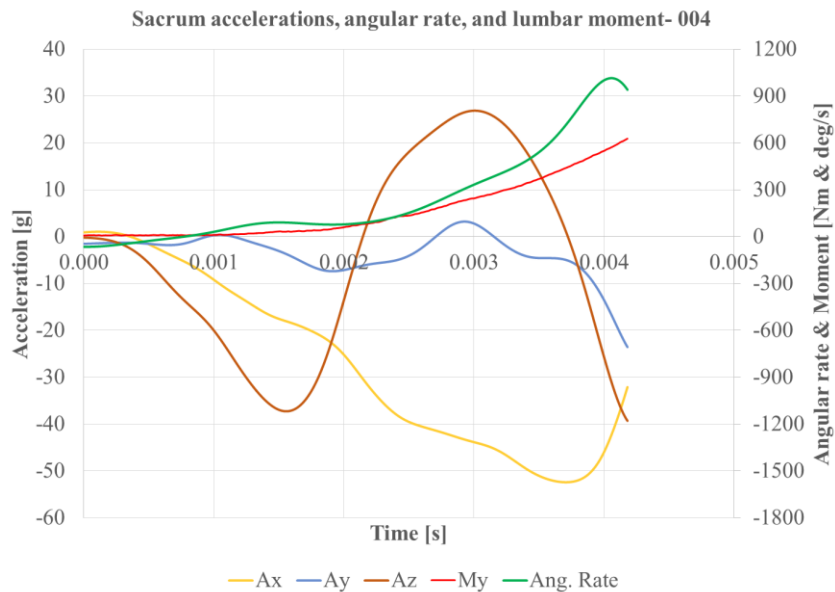


Figure 36 - Sacrum accelerations and angular rate, and pelvis moment about the y-axis for test 004. Az was negative until ~1.5ms and then turned to a positive trend before switching back to a negative trend at 3ms. Ax experienced acceleration in the negative direction and reached a minimum just before the angular rate sensor reached its peak.

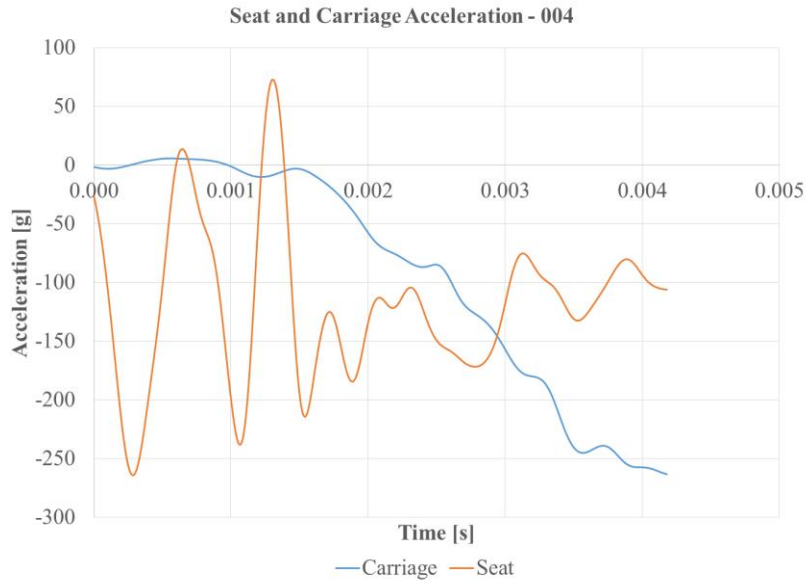


Figure 37 - Seat and carriage accelerations for test 004. The carriage does not start to accelerate until ~1.5ms.

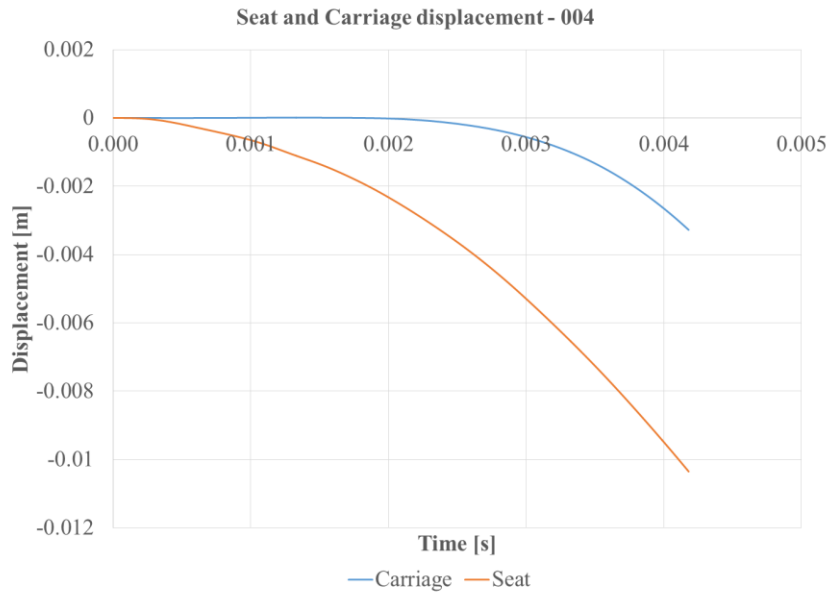


Figure 38 - Seat and carriage displacements for test 004. The displacements were calculated from double integrating the seat and carriage accelerometers. The total seat displacement was ~10mm.

Notes from post-test dissection:

Transverse fracture extending the length of the sacrum at the level of the inferior edge of the first sacral foramen. A vertical fracture beginning medial to the S1 vertebral body extending through the first sacral foramen to the left lateral edge of the sacrum at the level of the second foramen. Coccyx was noted to have two transverse fractures. Figure 39 shows a picture from the dissection of a fracture.

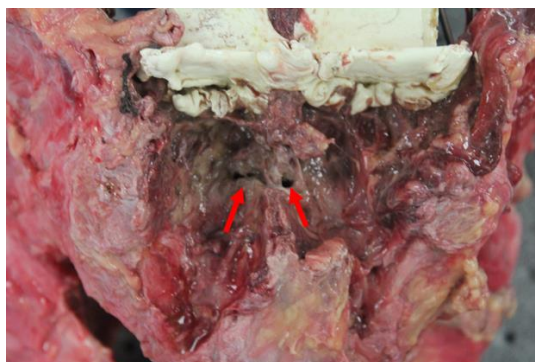


Figure 39 – Injury picture for test 004. The view of the posterior sacrum. Transverse fracture extending the length of the sacrum at the level of the inferior edge of the first sacral foramen.

Pelvis 005

Figure 40 shows the strain in the pelvis up to failure. The left SI gauge experienced the most compression. Its change in slope between 3.5 and 4 ms corresponds to a peak in angular rate and M_y in Figure 41. At about the same time, F_z exhibited unloading and then reloading. A_x , A_y , and A_z all experienced peaks just after 4 ms (Figure 42), which correspond to the reloading in F_z . After the peaks, the angular rate sensor recorded a faster change in rotation until failure was detected by the acoustic sensors.

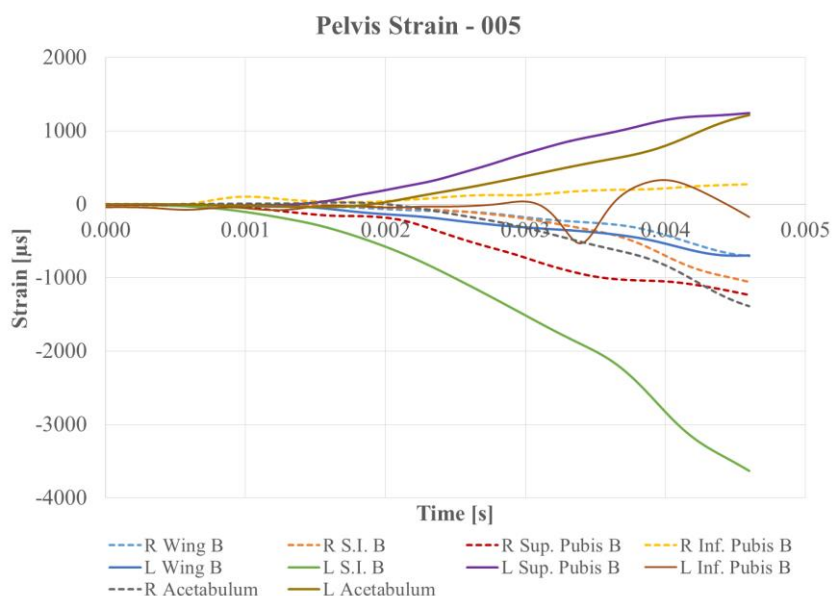


Figure 40 - Pelvis strains for test 005. The left and right S.I. gauges experienced the largest compressive strains.

Figure 43 and Figure 44 show the comparison between the seat and carriage accelerations, as well as the differences in overall displacements. The total distance that the seat moved before failure, as indicated by the acoustic sensor, was about 12 mm.

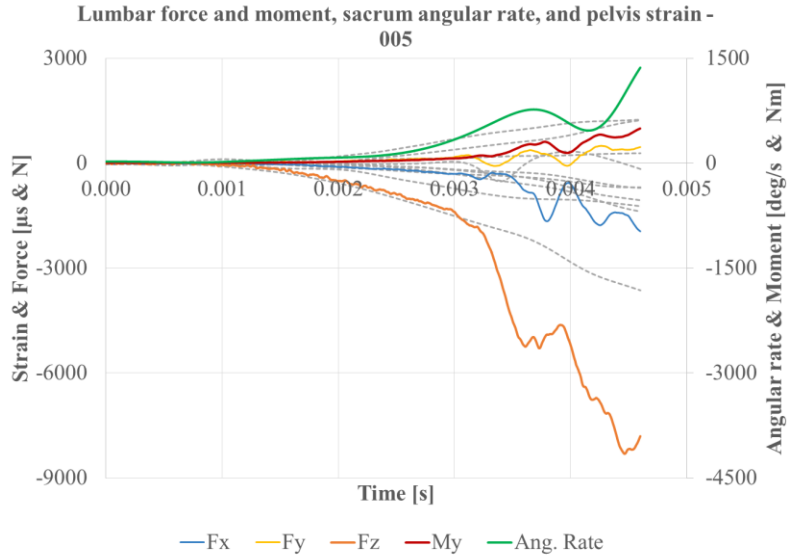


Figure 41 - Pelvis forces and moments, as well as sacrum angular rate for test 005. The gray dotted lines are the strains from the previous figure. Fz was the dominant force, and My and the angular rate sensor both had positive trends.

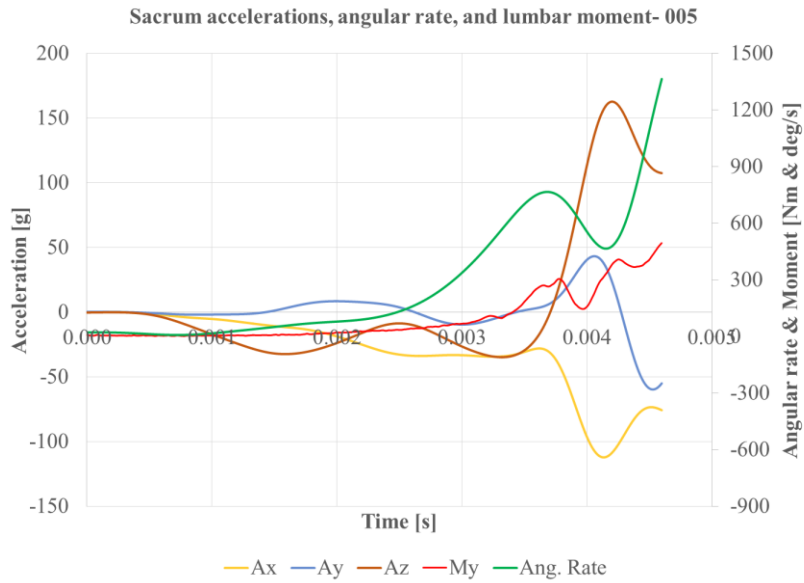


Figure 42 - Sacrum accelerations and angular rate, and pelvis moment about the y-axis for test 005. Ax, Ay, and Az all experienced peaks just after 4 ms, which correspond to the reloading in Fz. After the peaks, the angular rate sensor recorded a faster change in rotation until failure was detected by the acoustic sensors.

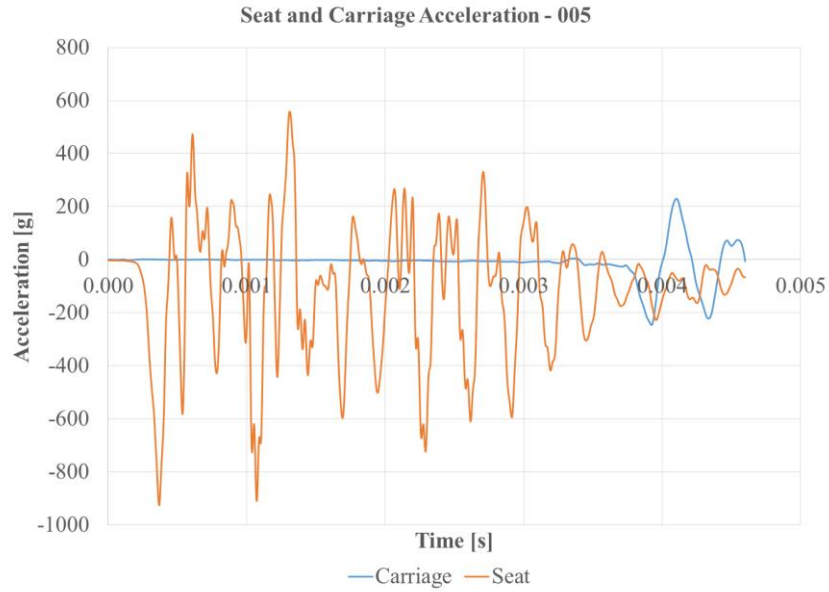


Figure 43 - Seat and carriage accelerations for test 005. The carriage does not start to accelerate until ~3ms. There is significant ringing in the seat accelerometer.

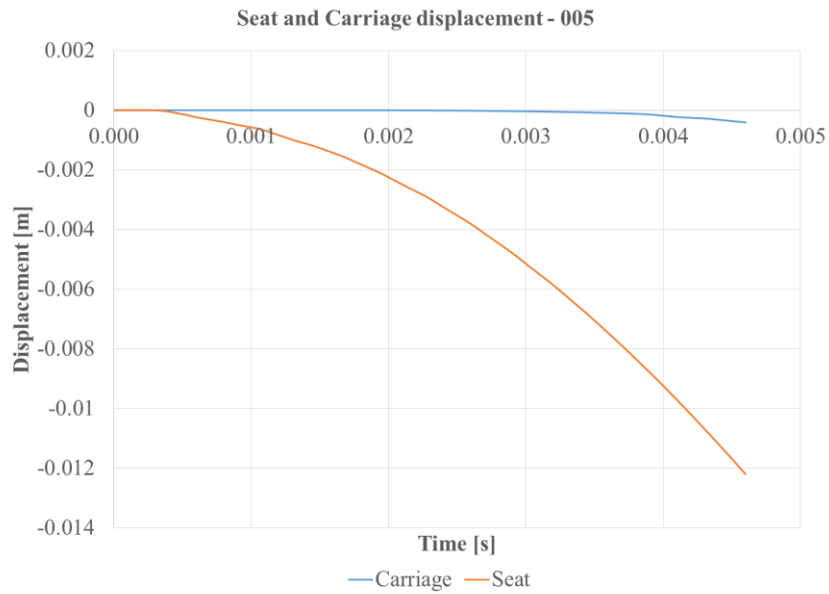


Figure 44 - Seat and carriage displacements for test 005. The displacements were calculated from double integrating the seat and carriage accelerometers. The total seat displacement was ~12mm.

Notes from post-test dissection:

Non-displaced right and left ischial spine fractures. Coccyx was noted to have two transverse fractures. Figure 45 shows a picture from the dissection of a fracture.

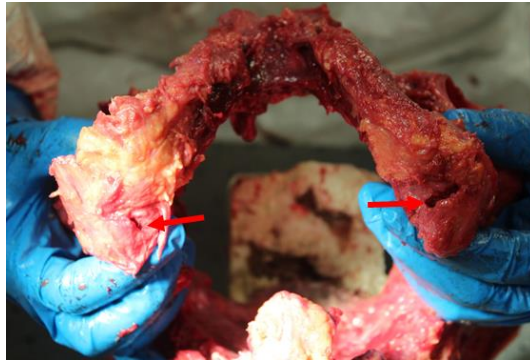


Figure 45 – Injury picture for test 005. Non-displaced right and left ischial spine fractures

Pelvis 006

Figure 46 shows the strain in the pelvis up to failure. The left SI gauge experienced the most compression. The right SI gauge experienced a compressive force too, but at a lesser magnitude than the left side. The left acetabulum experienced the most tension. The remainder of the gauges recorded primarily compressive strain.

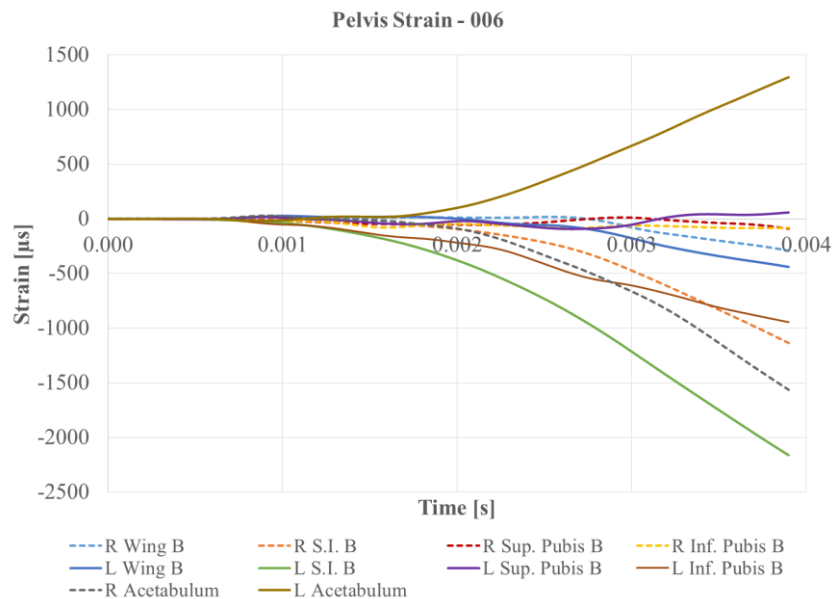


Figure 46 - Pelvis strains for test 006. The left S.I. gauge experienced the largest compressive strain.

Figure 47 shows the strain data as gray dotted lines with the pelvis forces and moment about the y-axis plotted in color. Fz was the dominant force, but there was a significant shear response along Fx. Lateral loading in Fy was minimal. The angular rate sensor peaked at about 3ms, which corresponds to an increase in the slope of My. Both the angular rate sensor and My had positive trends.

Figure 48 shows the negative and then positive acceleration response recorded by Az. Ax experienced acceleration in the negative direction and reached a minimum just after the angular rate sensor reached its peak. Minimal response from Ay suggests that there was minimal lateral loading.

Figure 49 and Figure 50 show the comparison between the seat and carriage accelerations, as well as the differences in overall displacements. The total distance that the seat moved before failure, as indicated by the acoustic sensor, was about 8 mm.

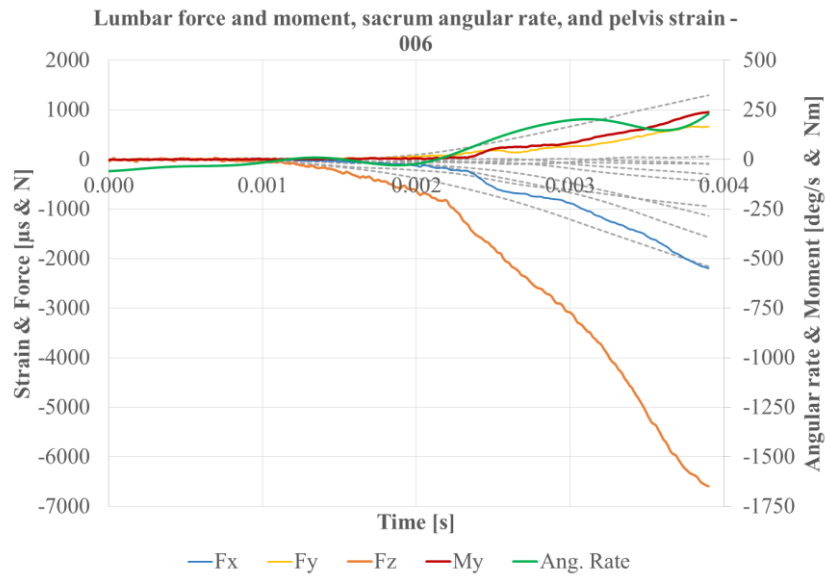


Figure 47 - Pelvis forces and moments, as well as sacrum angular rate for test 006. The gray dotted lines are the strains from the previous figure. Fz was the dominant force, and My and the angular rate sensor both had positive trends.

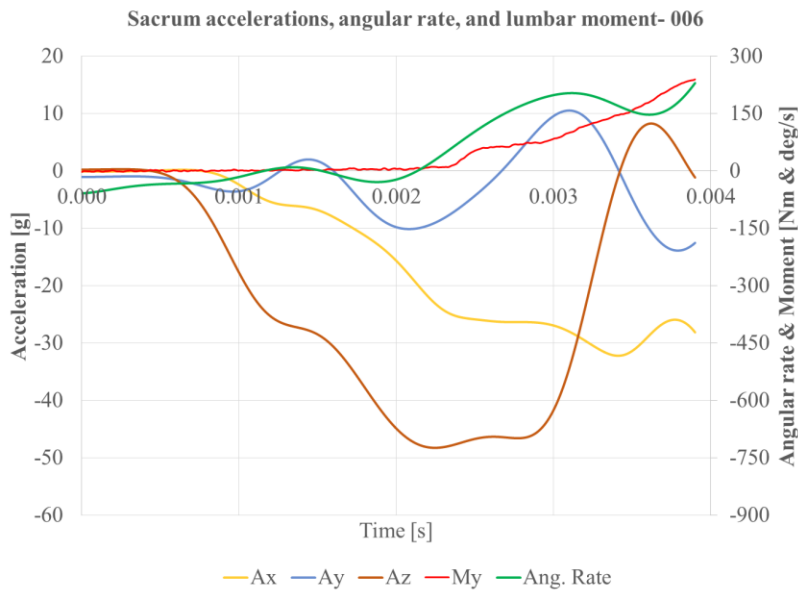


Figure 48 - Sacrum accelerations and angular rate, and pelvis moment about the y-axis for test 006. Az was negative until ~2.25ms and then turned to a positive trend before switching back to a negative trend at 3.5ms. Ax experienced acceleration in the negative direction and reached a minimum just after the angular rate sensor reached its peak.

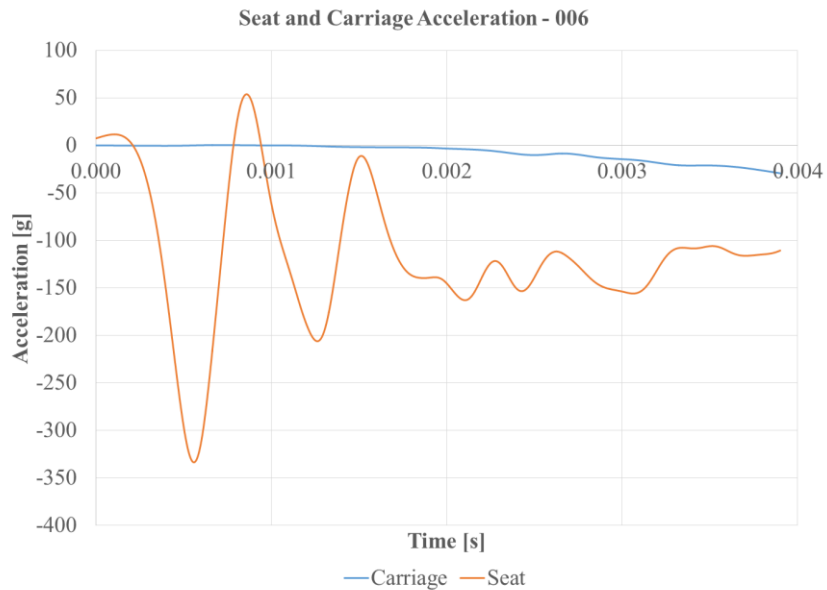


Figure 49 - Seat and carriage accelerations for test 006. The carriage does not start to accelerate until ~2ms.

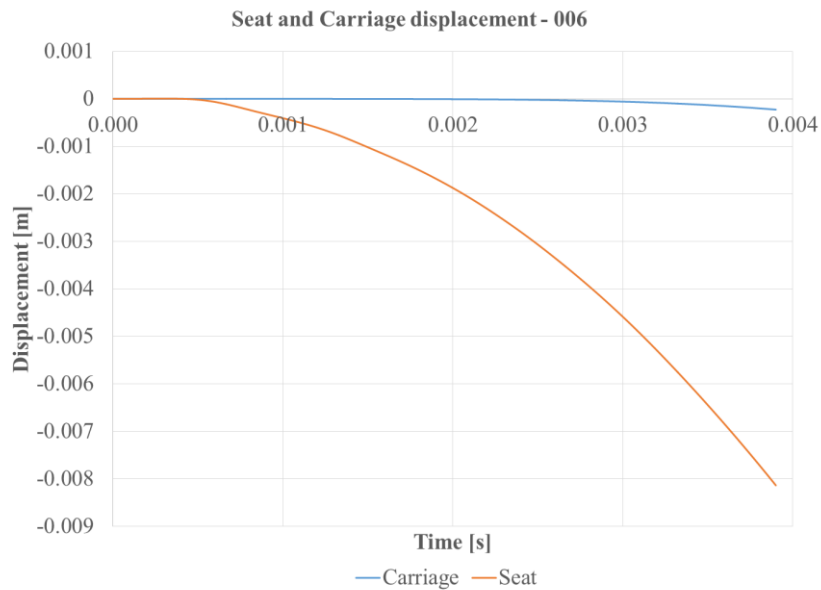


Figure 50 - Seat and carriage displacements for test 006. The displacements were calculated from double integrating the seat and carriage accelerometers. The total seat displacement was ~8mm.

Notes from post-test dissection:

Two vertical fractures of the right anterosuperior sacrum. The first followed the right SI joint, the second coursed medial of the SI vertebral body through the medial aspect of the right first foramen. There was a fracture of the left superior SI joint extending inferiorly to the level of the second foramen. A transverse fracture extended across the entire anterior sacrum at the level of

the second foramen. Comminuted coccyx fracture. Figure 51 shows a picture from the dissection of a fracture.

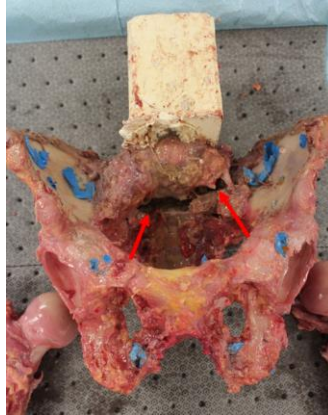


Figure 51 – Injury picture for test 006. A transverse fracture extended across the entire anterior sacrum at the level of the second foramen.

Pelvis 007

Figure 52 shows the strain in the pelvis up to failure. The left and right SI gauges experienced the most compression. The left superior pubis and right inferior pubis experienced the most tension, with the left acetabulum experiencing a lesser degree of tension. The remainder of the gauges recorded primarily compressive strain.

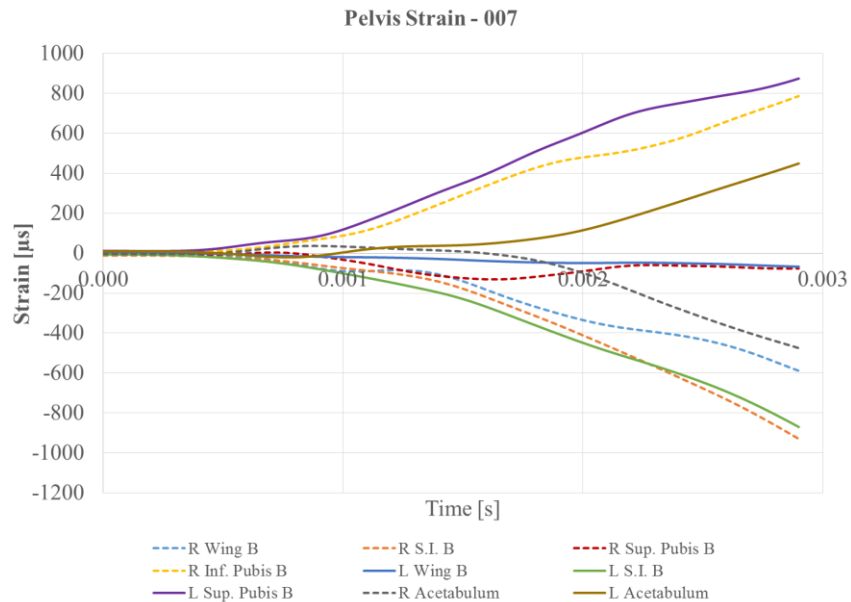


Figure 52 - Pelvis strains for test 007. The left and right S.I. gauges experienced the largest compressive strains.

Figure 53 shows the strain data as gray dotted lines with the pelvis forces and moment about the y-axis plotted in color. Fz was the dominant force, but there was a slight shear response along Fx. Fy, My, and the sacrum data were unsuccessfully recorded on this test.

Figure 54 and Figure 55 show the comparison between the seat and carriage accelerations, as well as the differences in overall displacements. The total distance that the seat moved before failure, as indicated by the acoustic sensor, was about 5 mm.

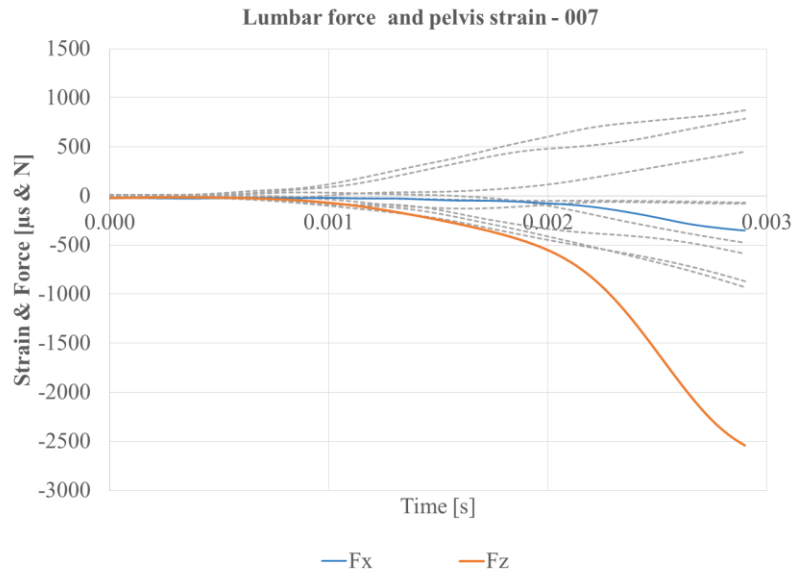


Figure 53 - Pelvis Fx and Fz for test 007. The gray dotted lines are the strains from the previous figure. Fz was the dominant force and reached over 2.5kN before failure.

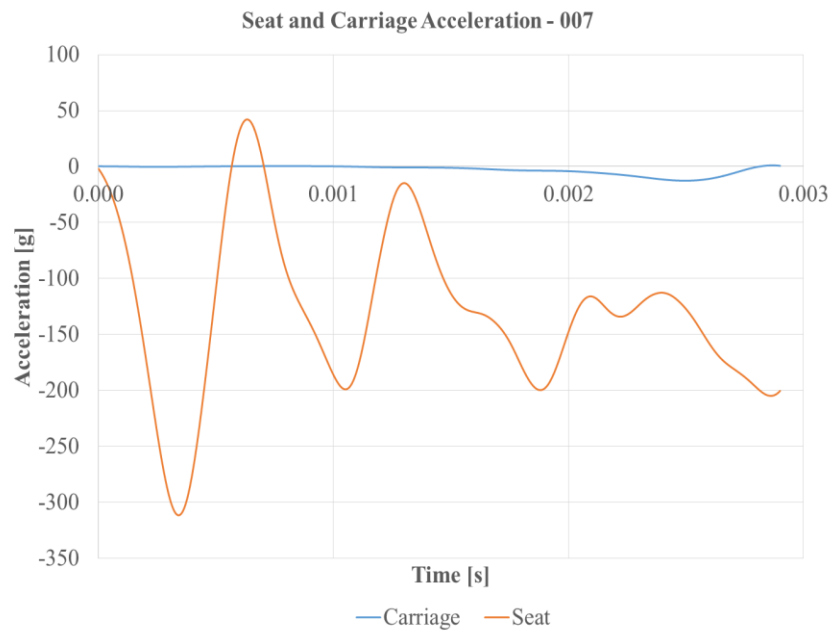


Figure 54 - Seat and carriage accelerations for test 007. The carriage does not start to accelerate until ~1.75ms.

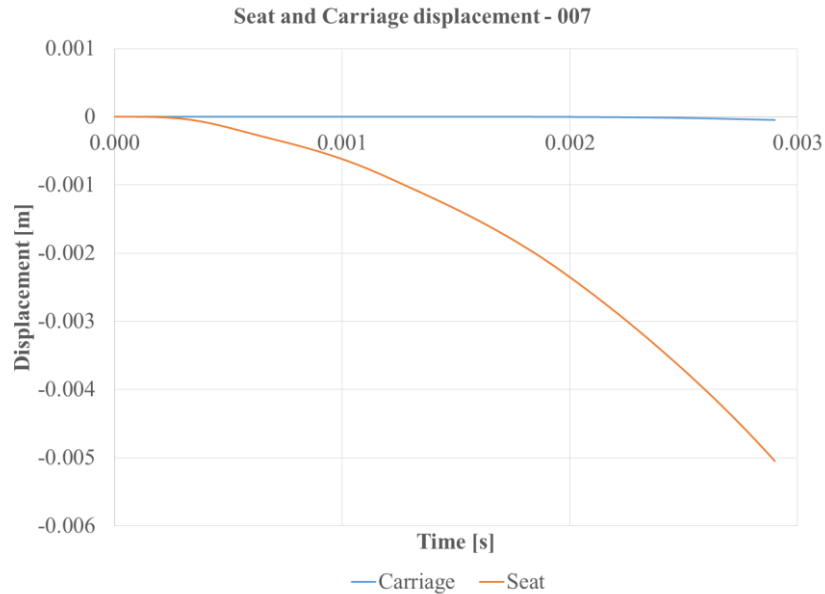


Figure 55 - Seat and carriage displacements for test 007. The displacements were calculated from double integrating the seat and carriage accelerometers. The total seat displacement was ~5mm.

Notes from post-test dissection:

Vertical fracture that followed the right SI joint which then coursed medially through the lateral aspect of the first foramen then the medial aspect of the second foramen. A second vertical fracture began approximately midway between the SI vertebral body and the left SI joint. Transverse fracture between the first foramen. Transverse fracture between the second foramen.
 Figure 56 shows a picture from the dissection of a fracture.



Figure 56 – Injury picture for test 007. Transverse fracture between the first foramen.

Pelvis 008

Figure 57 shows the strain in the pelvis up to failure. The left and right SI gauges experienced the most compression. The left acetabulum and right superior pubis experienced the most tension. The left and right superior pubis gauges reached their peak magnitudes between 3 and 3.5ms, which corresponds to an increase in loading rate as well as an increase in moment rate.

Figure 58 shows the strain data as gray dotted lines with the pelvis forces and moment about the y-axis plotted in color. Fz was the dominant force, but there was a significant shear response from Fx. Lateral loading in Fy was minimal. Both the angular rate sensor and My had positive trends.

Figure 59 shows the negative and then positive acceleration response recorded by Az. Ax experienced acceleration in the negative direction and reached a minimum at about 3.5 ms. A minimal response in Ay suggests that there was minimal lateral loading.

Figure 60 and Figure 61 show the comparison between the seat and carriage accelerations, as well as the differences in overall displacements. The total distance that the seat moved before failure, as indicated by the acoustic sensor, was about 8 mm.

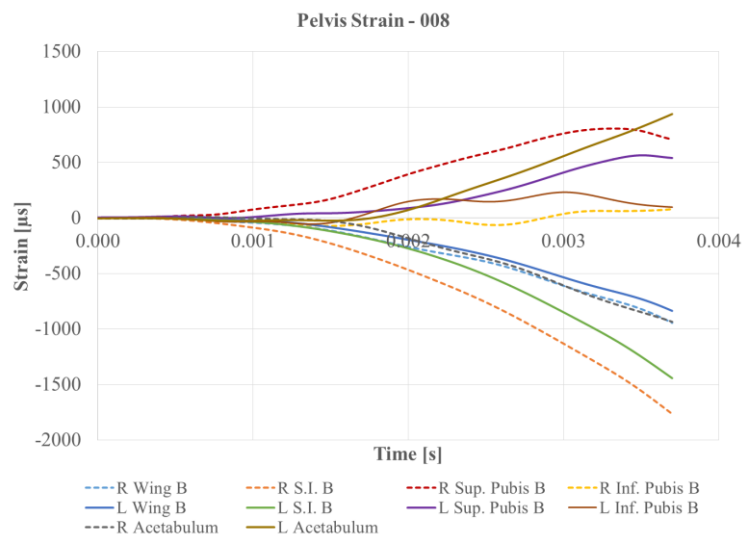


Figure 57 - Pelvis strains for test 008. The left and right S.I. gauges experienced the largest compressive strains.

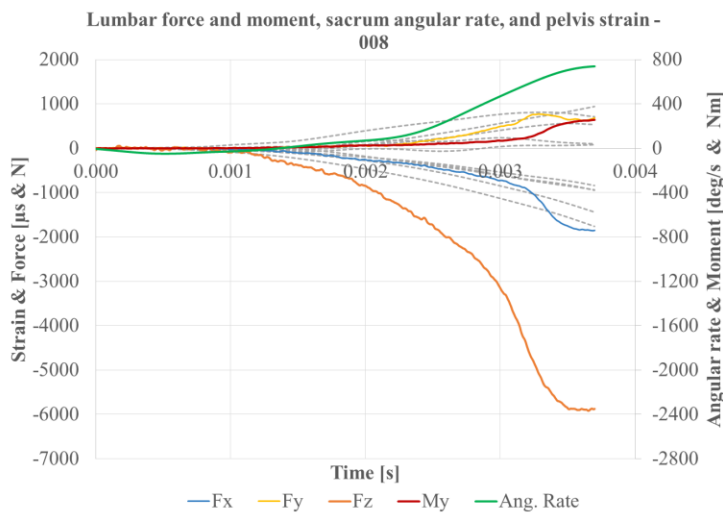


Figure 58 - Pelvis forces and moments, as well as sacrum angular rate for test 008. The gray dotted lines are the strains from the previous figure. Fz was the dominant force, and My and the angular rate sensor both had positive trends.

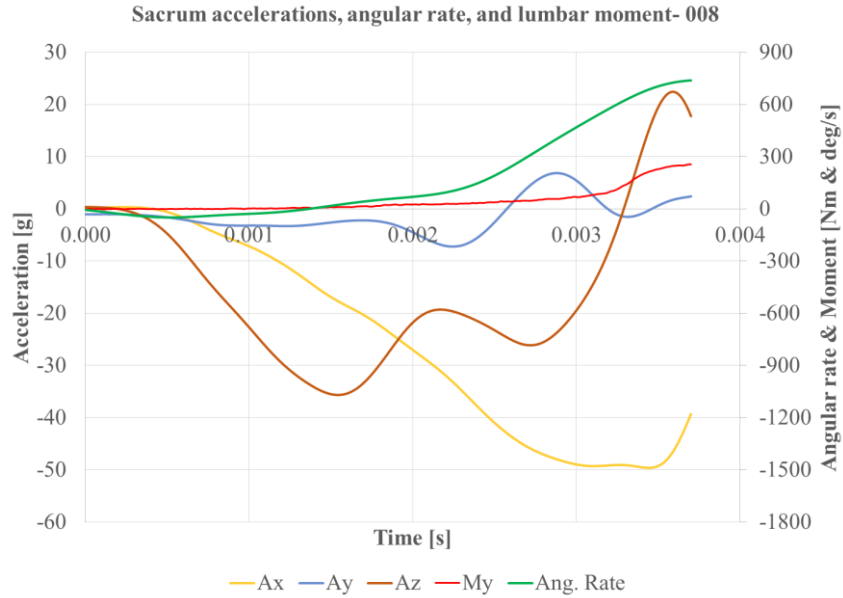


Figure 59 - Sacrum accelerations and angular rate, and pelvis moment about the y-axis for test 008. Az was negative until ~1.5ms. Ax experienced acceleration in the negative direction and reached a minimum just before the angular rate sensor reached its peak.

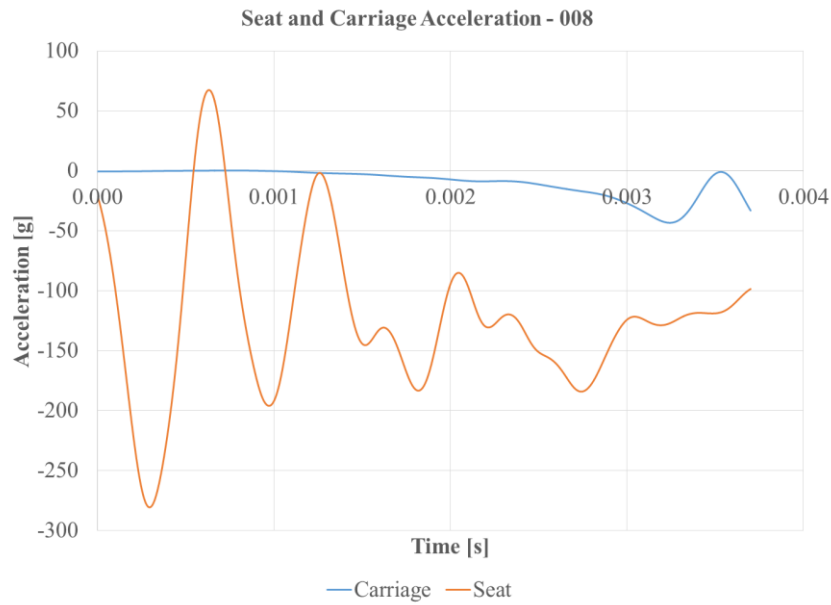


Figure 60 - Seat and carriage accelerations for test 008. The carriage does not start to accelerate until ~1.5ms.

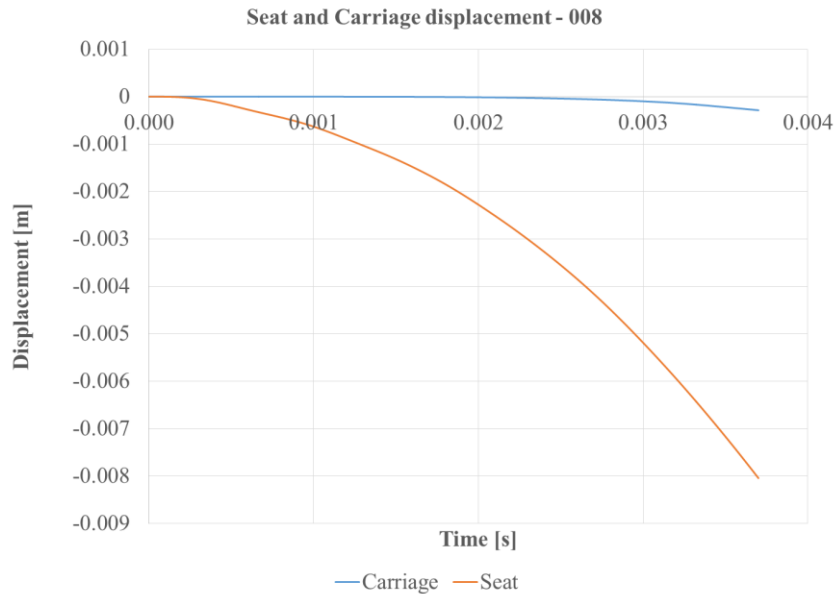


Figure 61 - Seat and carriage displacements for test 008. The displacements were calculated from double integrating the seat and carriage accelerometers. The total seat displacement was ~8mm.

Notes from post-test dissection:

Two vertical fractures extending both lateral aspects of the vertebral column inferior to the first ipsilateral sacral foramen. There was transverse fracture extending between the first sacral foramen. Coccyx was noted to have two transverse fractures. Figure 62 shows a picture from the dissection of a fracture.



Figure 62 – Injury picture for test 008. There was transverse fracture extending between the first sacral foramen.

Pelvis 009

Figure 63 shows the strain in the pelvis up to failure. The left and right SI gauges experienced nearly identical compression, as well as the left and right wings. The right inferior pubis gauge measured a large tensile strain at about 3.75 ms.

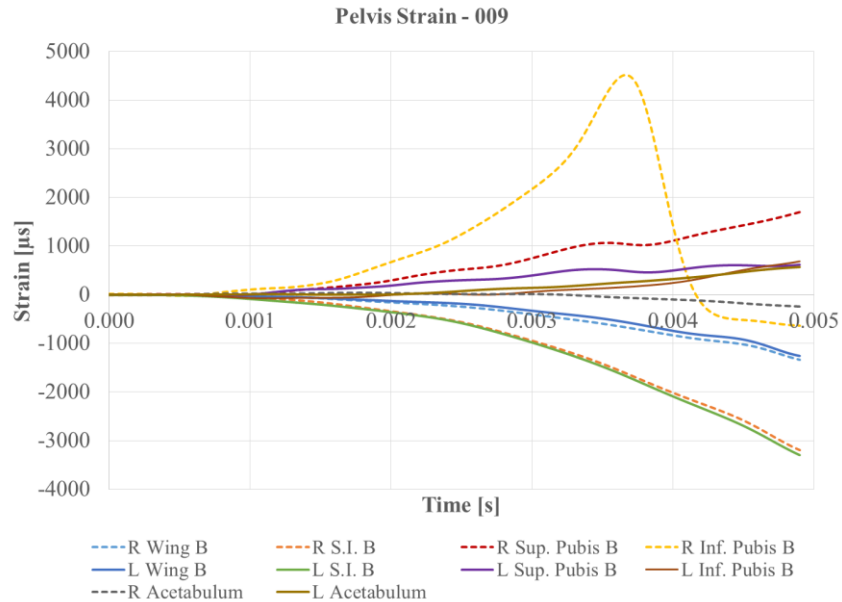


Figure 63 - Pelvis strains for test 009. The left and right S.I. gauges experienced the largest compressive strains. The large peak measured by the right inferior pubis gauge is attributed to a localized fracture diagnosed in the post-test dissection.

Figure 64 shows the strain data as gray dotted lines with the pelvis forces and moment about the y-axis plotted in color. Fz was the dominant force, but there was about a 2 kN shear load in Fx. Lateral loading in Fy was minimal. Both the angular rate sensor and My had positive trends. Fz experienced a loading phase up to about 3.75 ms before it unloaded and reloaded just after 4ms. The initial unloading corresponds to the peak in the strain at the right inferior pubis gauge. The injury note below indicates that the ischial tuberosities were fractured, thus the axial unloading and peak in strain can be attributed to this injury before the sacrum experiences its significant failure at 4.9 ms.

Figure 65 shows the negative and then positive acceleration response recorded by Az. Ax experienced acceleration in the negative direction and reached a minimum at about 4.5 ms. Minimal response from Ay suggests that there was minimal lateral loading. The peaks in angular rate, Ay, and Az after 4 ms likely reflect the sacrum starting to fail.

Figure 66 and Figure 67 show the comparison between the seat and carriage accelerations, as well as the differences in overall displacements. The total distance that the seat moved before failure, as indicated by the acoustic sensor, was about 14 mm.

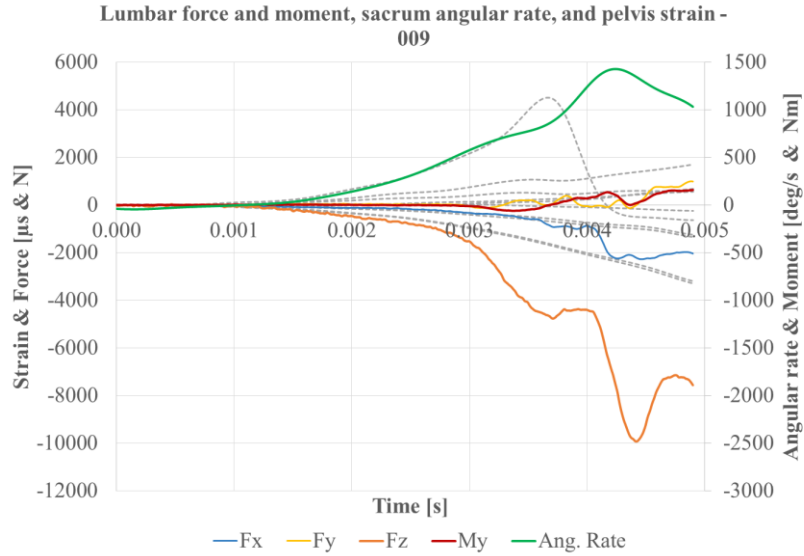


Figure 64 - Pelvis forces and moments, as well as sacrum angular rate for test 009. The gray dotted lines are the strains from the previous figure. As the dominant force, experienced a loading phase up to about 3.75 ms before it unloaded and reloaded, which corresponds to the peak in the right inferior pubis gauge and reflects fracture in the ischial tuberosities. My and the angular rate sensor both had positive trends.

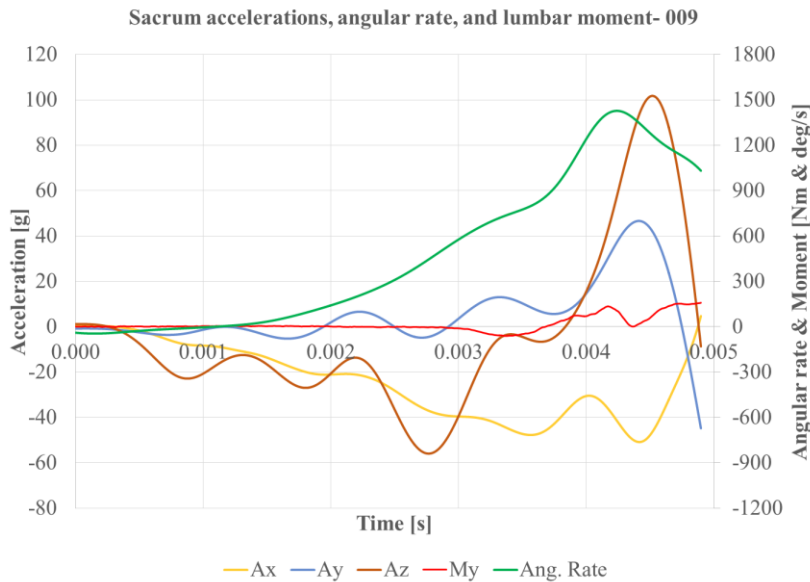


Figure 65 - Sacrum accelerations and angular rate, and pelvis moment about the y-axis for test 009. Ax, Ay, and Az all experienced peaks just after 4 ms, which correspond to the reloading in Fz and likely represent failure in the sacrum.

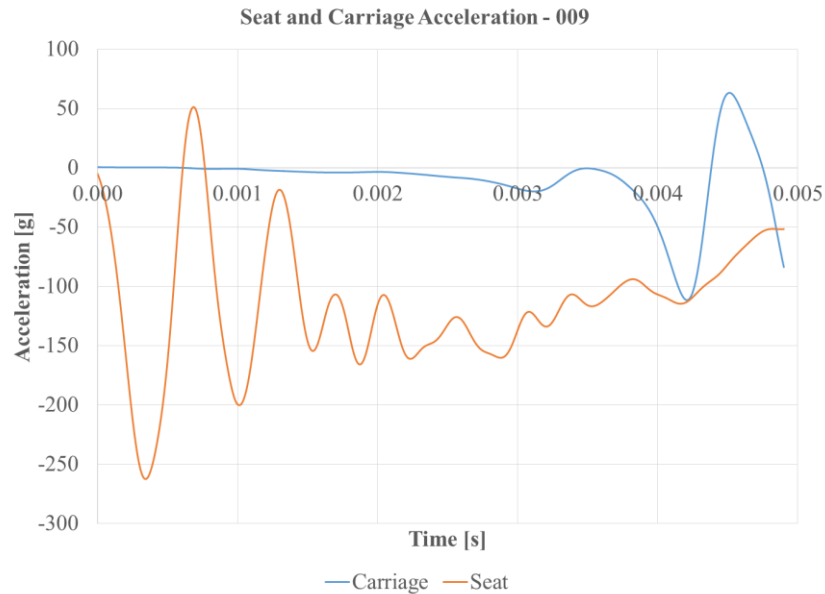


Figure 66 - Seat and carriage accelerations for test 009. The carriage does not start to accelerate until ~1.5ms.

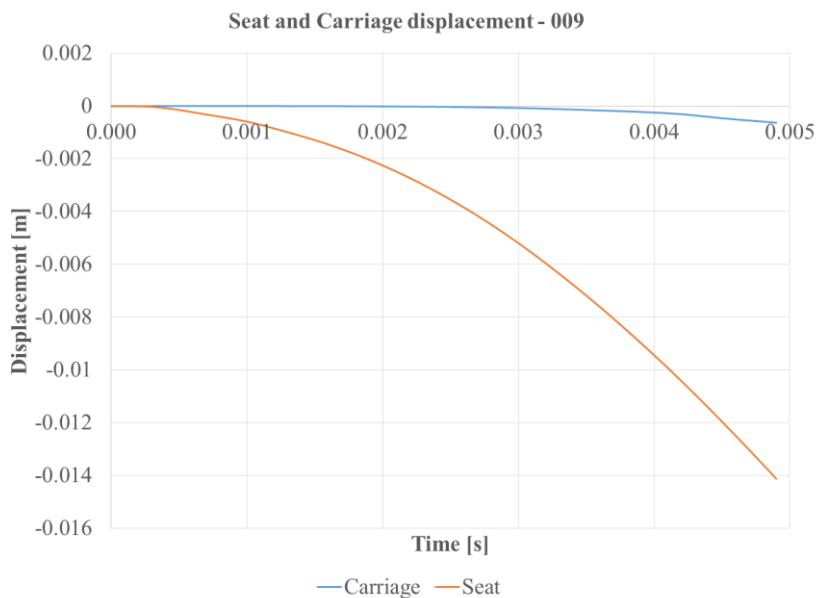


Figure 67 - Seat and carriage displacements for test 009. The displacements were calculated from double integrating the seat and carriage accelerometers. The total seat displacement was ~14mm.

Notes from post-test dissection:

Fracture extending inferiorly from the medial aspect of the superior sacrum. The fracture line passed through the first and second sacral foramen then traveled to the left anterior edge of the sacrum at the level of the fourth foramen. Comminuted fracture bilateral ischial tuberosities. Comminuted fracture of coccyx. Figure 68 shows a picture from the dissection of a fracture.

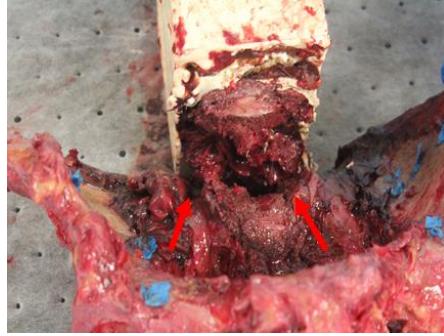


Figure 68 – Injury picture for test 009. The fracture line passed through the first and second sacral foramen then traveled to the left anterior edge of the sacrum at the level of the fourth foramen.

Pelvis 010

Figure 69 shows the strain in the pelvis up to failure. The left inferior pubis gauge failed and no data is presented. The left SI gauge experienced the most compression, followed by the right SI gauge. The left acetabulum experienced the most tension, followed by the left superior pubis and right inferior pubis. There were no dramatic shifts in the strain responses to suggest failures or load shifting.

Figure 70 shows the strain data as gray dotted lines with the pelvis forces and moment about the y-axis plotted in color. Fz was the dominant force, but there was a 1.5 kN shear force along Fx. Lateral loading in Fy was minimal. Both the angular rate sensor and My had positive trends, but the angular rate sensor reached a peak before the end of the trace at about 3.4 ms.

Figure 71 shows the negative and then positive acceleration response recorded by Az. Ax experienced acceleration in the negative direction and then peaked with positive acceleration at the time of failure. A minimal response from Ay suggests that there was minimal lateral loading up to failure.

Figure 72 and Figure 73 show the comparison between the seat and carriage accelerations, as well as the differences in overall displacements. The total distance that the seat moved before failure, as indicated by the acoustic sensor, was about 8 mm.

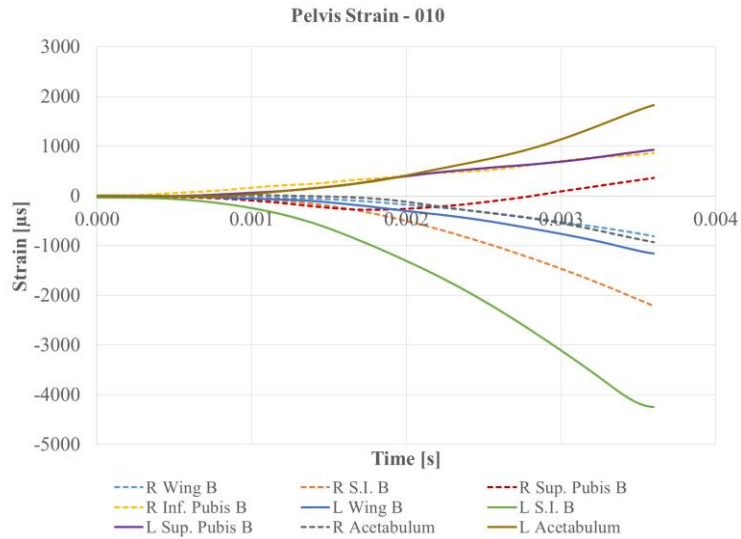


Figure 69 - Pelvis strains for test 010. The left and right S.I. gauges experienced the largest compressive strains.

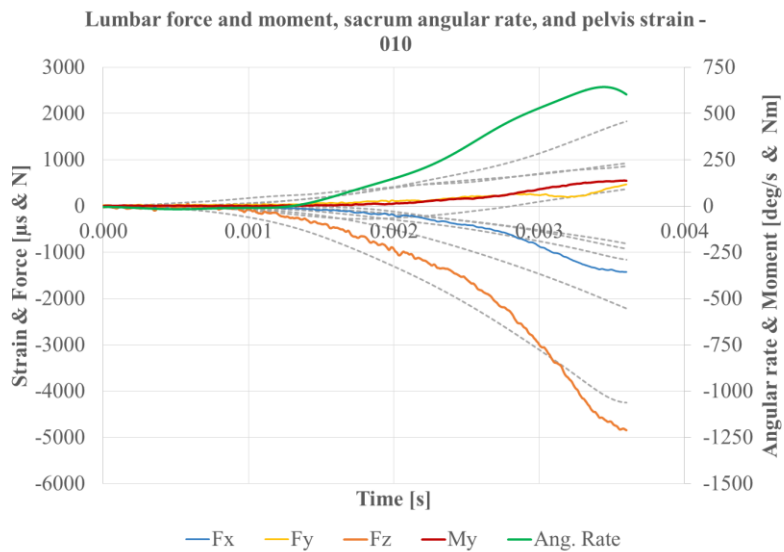


Figure 70 - Pelvis forces and moments, as well as sacrum angular rate for test 010. The gray dotted lines are the strains from the previous figure. Fz was the dominant force, and My and the angular rate sensor both had positive trends.

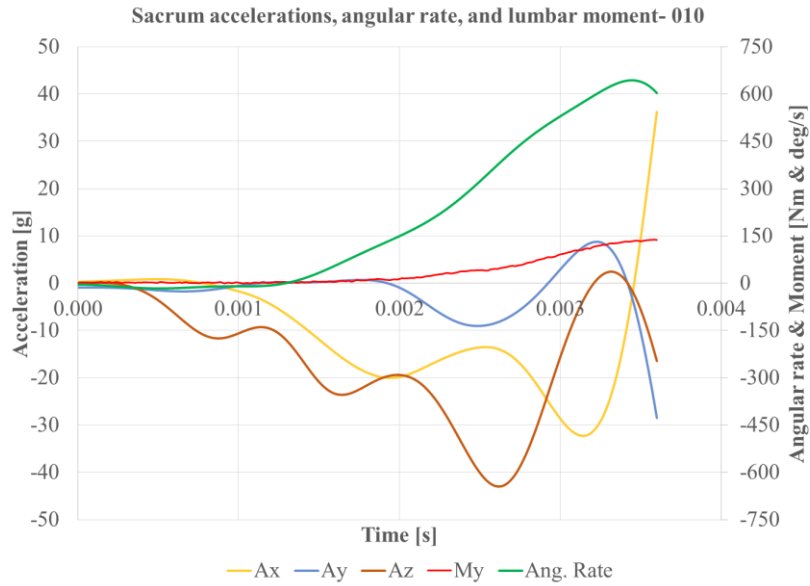


Figure 71 - Sacrum accelerations and angular rate, and pelvis moment about the y-axis for test 010. Az was negative until ~2.5ms and then turned to a positive trend before switching back to a negative trend at 3.25ms. Ax experienced acceleration in the negative direction and reached a minimum just before the angular rate sensor reached its peak.

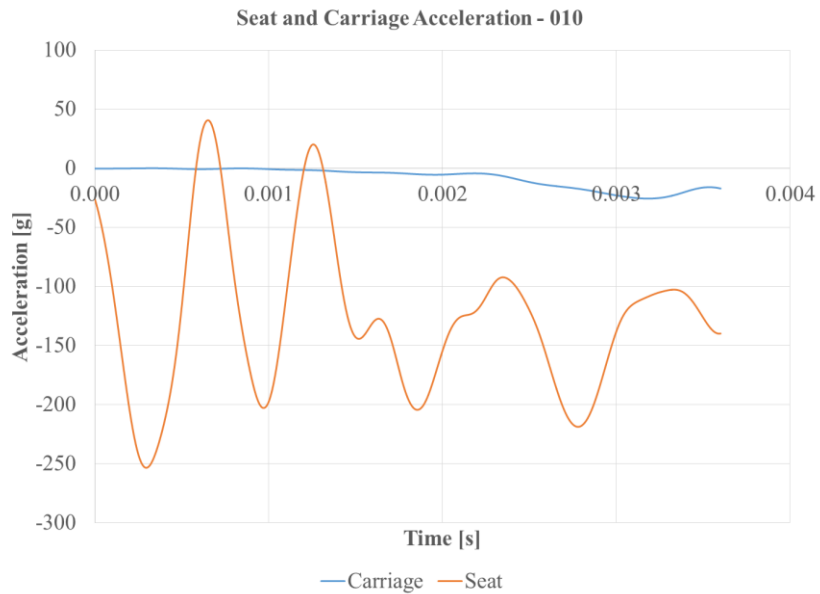


Figure 72 - Seat and carriage accelerations for test 010. The carriage does not accelerate until ~1.75ms.

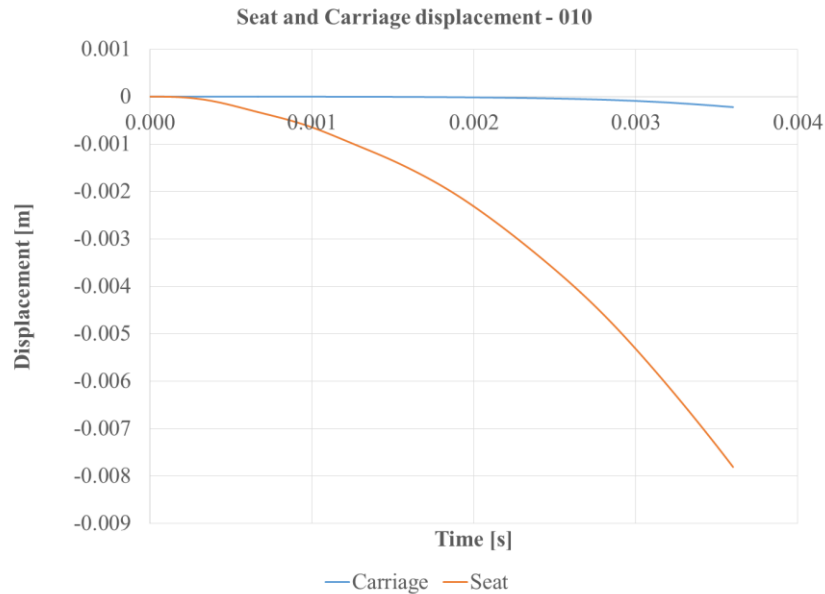


Figure 73 - Seat and carriage displacements for test 010. The displacements were calculated from double integrating the seat and carriage accelerometers. The total seat displacement was ~8mm.

Notes from post-test dissection:

Transverse fracture at the level of the inferior edge of the first sacral foramen. Vertical fracture extended to the level of the first foramen bilaterally. Coccyx was noted to have two transverse fractures of the proximal segment. Figure 74 shows a picture from the dissection of a fracture.

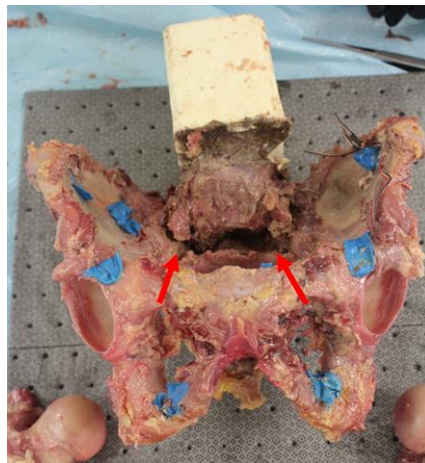


Figure 74 – Injury picture for test 010. Transverse fracture at the level of the inferior edge of the first sacral foramen.

DISCUSSION

Boundary Conditions

The boundary conditions on Telemachus were designed to be rigid and constrained to move along a single axis. Although the specimens failed at the potting interface, the data up to the point of failure is reliable. The simplified single-axis loading condition was necessary in order to gain a basic understanding of the pelvic response along the axial direction before trying to understand a complex, unconstrained input force. Additionally, the rigid boundary at the

superior side of the pelvis takes the place of a flexible lumbar spine and compliant vertebral discs. The rigidity introduced stress concentrations and led to failure at the potting interface. Future testing should explore alternative methods for holding on to the pelvis.

Future testing should also consider evaluating the sensitivity of force response to the carriage mass by varying or eliminating the carriage mass or fixing the superior boundary. Since mass is recruited dynamically, the fixed carriage mass used in this study was only representative of the mass at the peak pelvis acceleration in the MADYMO model.

Force-Response Corridors

Figure 75 and Figure 76 show the resulting response corridors calculated for Pelvis Fz and Pelvis My. The characteristic average trace is a red line and the response corridor boundaries are dashed black lines. The traces from the tests are grayed out within the corridor.

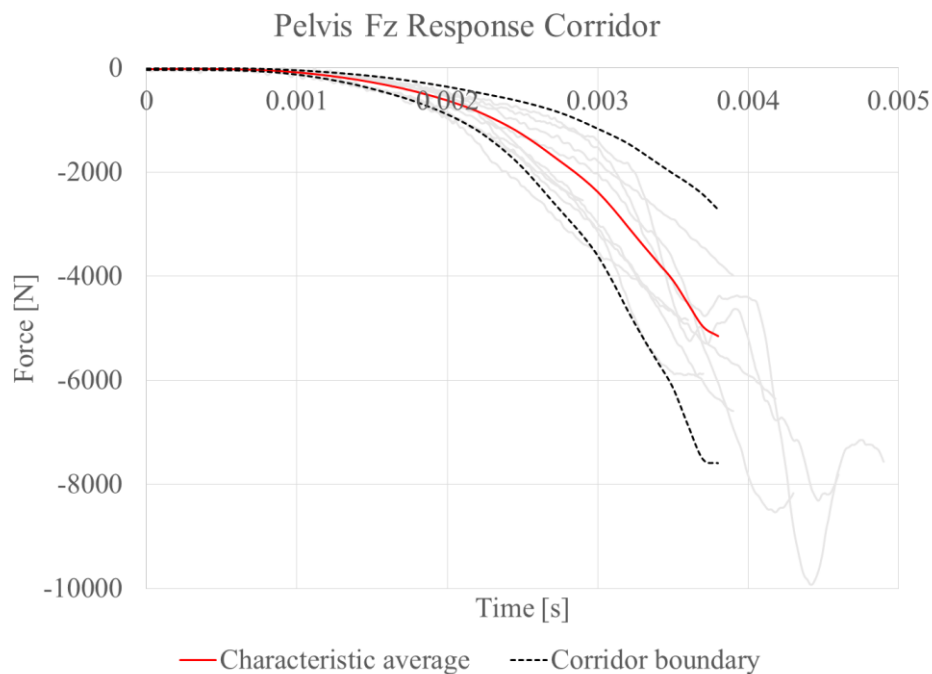


Figure 75 – Response corridor of Fz forces. The red line is the calculated characteristic average and the dotted black lines are the bounds of the corridor. The light gray lines are the data traces that Fz data traces that are terminated at time of failure.

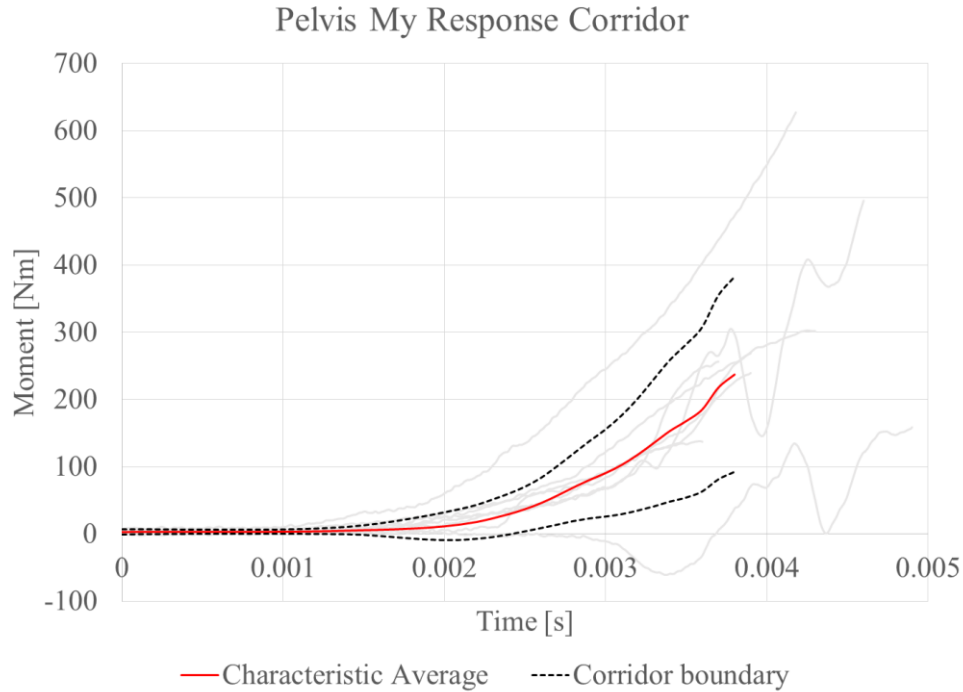


Figure 76 - Response corridor of My moments. The red line is the calculated characteristic average and the dotted black lines are the bounds of the corridor. The light gray lines are the data traces that My data traces that are terminated at time of failure.

Axial Force-Displacement

The seat and carriage accelerations (global coordinate system) at the inferior and superior boundary of the pelvis were double integrated to calculate displacements. Figure 77 shows the resulting response corridor for the force-displacement data.

A linear relationship was assumed to calculate the axial stiffness for each specimen. The stiffness was calculated by taking the slope between the point representing 80% of the fracture force and 20% of the fracture force. Table 9 summarizes the axial stiffness values for each test.

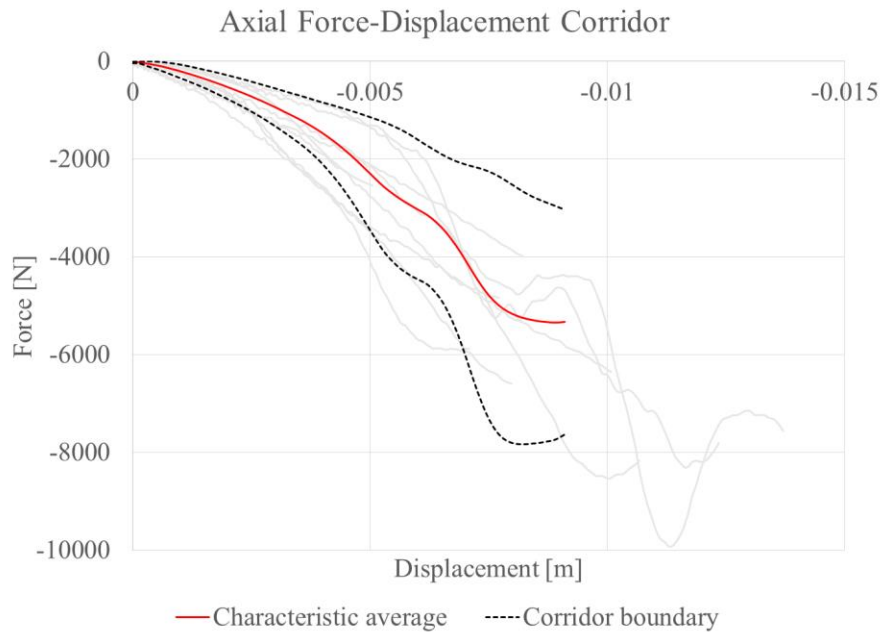


Figure 77 – Axial force-displacement plots up to fracture. A linear relationship was assumed for the stiffness calculation. The light gray lines are force-displacement traces that are terminated at time of failure.

Table 9 – Summary of calculated axial stiffness values.

Test #	Calculated Axial Stiffness (kN/m)
UVA_PELVIS_001	-
UVA_PELVIS_002	547
UVA_PELVIS_003	1144
UVA_PELVIS_004	756
UVA_PELVIS_005	1094
UVA_PELVIS_006	1042
UVA_PELVIS_007	1054
UVA_PELVIS_008	1133
UVA_PELVIS_009	991
UVA_PELVIS_010	744
average (003-010)	995
standard deviation	159

Pelvis/Sacrum Response

The test starts as the seat begins to load the inferior pelvis (Figure 78). Immediately after, strains are observed throughout the pelvis, as well as an axial and shear force response along the z- and x-axis, followed by rotation and acceleration on the sacrum. The strain data show that the load causes a shear force at the SI joints, as evidenced by the compression recorded along the joints (Figure 79). The resulting fractures indicate that there are two primary load

paths through the pelvis. Coccyx fractures indicate distal sacrum loading, while ischial tuberosity and ischial spine fractures indicate distal ischium loading. Table 10 organizes the tests into categories based on distal fractures and shows that a majority of the specimens experienced a distal sacrum fracture, while a smaller number experience both an ischium and distal sacrum fracture. It should be noted that even though the ischium were not fractured in all cases, the strain data proves that loading occurred. Also, the majority of the specimens sustained a proximal sacrum fracture that could have been initiated by either load path. Since there is no way to discern how the load is distributed between the two paths in these tests, the calculated stiffness values in Table 9 may be a combined representation of both paths.

Table 10 – Distal pelvis fractures categorized to show two primary load paths.

Distal Fracture Location	Test number
Distal sacrum (e.g. coccyx) only	003, 004, 006, 008, 010
Ischium & distal sacrum	002, 005, 009

The increase in compression rate of Fz can be attributed to the sacrum nearing the limit of its range of motion in bending, thus causing more resistance and an increase in compressive force as well as an increase in shear and moment.

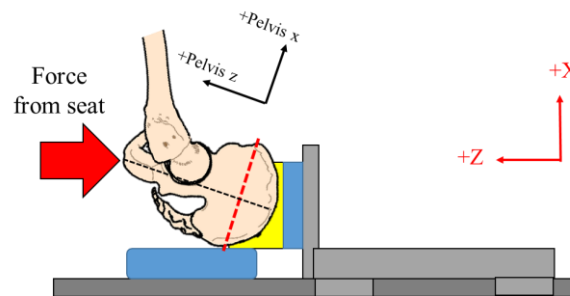


Figure 78 – Schematic of the pelvis being loaded by the seat.

Flexing is seen in the ilium and pubic regions, but the fractures occur in the sacrum. The compressed soft tissue between the seat and sacrum, continues to load the sacrum until there is a failure. The curved geometry of the sacrum, together with its initial position facing the incoming load, can explain the positive trend of the angular rate and moments (Figure 80).

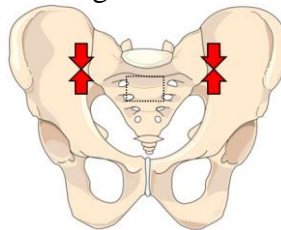


Figure 79 – Schematic of the pelvis indicating the areas of high compressive strain adjacent to the SI joints.

The strain elements recorded a wide range of strains throughout the pelvis. The left and right SI gauges always experienced compressive strains and usually were the largest in magnitude. It should be noted that the variance in response amongst some of the other gauges, especially the acetabulum and pubis gauges (inferior and superior), can be attributed to alignment/positioning challenges due to accessibility constraints.

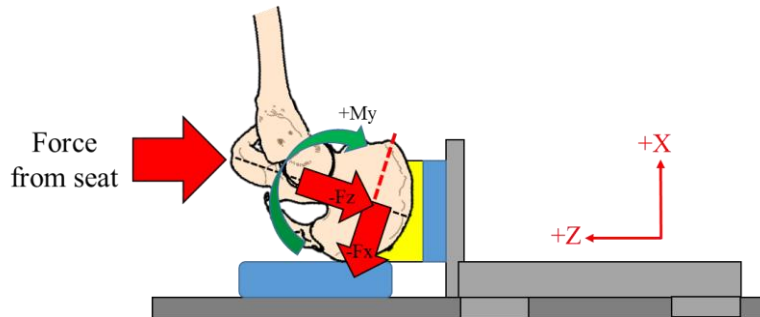


Figure 80 – Schematic of the axial and shear forces experienced by the pelvis, as well as the positive moment about the y-axis.

Fractures and Stiffness

As mentioned, the fractures seen in the pelvis were likely caused by the stress concentrations introduced by the mounting hardware (screws and rigid FastCast). While a few of the injuries reported are representative of realistic injuries seen in combat theater (i.e. coccyx fractures and localized ischial tuberosity fractures), the majority of the injuries sustained in this study are not.

Since failure force and time were determined using the acoustic sensors in this study, the response of the pelvis up to that point is usable data for ATD and model development. Test 009 proved to be unique in that a local ischial tuberosity fracture was detected on a strain gauge before the acoustic sensors detected fracture (Figure 63 and Figure 64). This was atypical in this study since no other failures were detected by strain gauges.

The loading rate and the pelvis kinematic response are important results that ATD developers and modelers alike can use for model development. The strain gauge data proved that the pelvis was being deformed during the loading phase and not just being pushed down the track as a rigid body.

The boundary data were used to calculate axial stiffness. A linear response was assumed for the calculations, and it is acknowledged that there is an inertial component in the force response data that cannot be eliminated with the data collected in this study. The development of a lumped-mass model of the pelvis would help determine the sensitivity to the distributed mass and its effect on force response. The stiffness values calculated do reveal a more rigid response than previous studies that loaded the pelvis in the lateral and frontal directions. Specifically, Chamouard reported a 300 kN/m dynamic stiffness value for the pelvis, which is about one-third of the stiffness calculated in this study. The force at failure recorded in this study tends to agree with the static fracture forces reported by Chamouard and the dynamic force reported by Salzar (Chamouard 1993; Salzar 2006), but could merely be a coincidence. Future studies that eliminate the failure at the pot will be able to report more reliable forces at fracture.

Similarly to axial stiffness, a calculated rotational stiffness was explored. However, it was determined that the rotational data from the sacrum was not representative of the rest of the pelvis and therefore could not be used for a reliable calculation. Therefore, use of the additional gauges listed in the limitations section is warranted for future studies to quantify the rotational stiffness of the pelvis. The addition of the gauges will also help separate axial and bending stiffnesses due to the ability to calculate axial translations as a result of the rotations.

Axial and shear moment arms

Because the load cell and seat positions are fixed along the X-axis, except for slight adjustments that can be made at the load cell to accommodate varying anatomical geometries,

the distance between their respective centers is known. Since the relationship between the pelvis coordinate system and the load cell center is known, it was determined that the calculated Fz moment arm, dX , was approximately in line with the center of the seat. Since the failure occurred during the loading phase of the seat accelerometer, the primary force vector should still be coming from the center of the seat.

Limitations

While this study was the first of its kind, future studies should improve the method for rigidly holding onto the pelvis. Specifically, an alternative method to eliminate the compliance of the vertebral discs and not introduce a stress concentration needs to be developed. The rigid potting method used in this study proved to cause local stress concentrations in the sacrum and resulted in failure at the interface in each test.

The calculated axial stiffness for the second test (potted at a -45° angle) is less than the stiffness calculated at a -22° angle and has a greater moment about the y-axis at failure. While this is only one case, it may suggest that the stiffness values depend on pelvis position. More tests are needed to further prove or disprove that notion. Additional loading rates should also be investigated so that there is a better understanding of the pelvis response across a wider spectrum of loading rates.

Additional strain gauges should be used on the sacrum to measure local deformations and quantify flexing in that region. Six-axis motion blocks should be used on both the sacrum and pubic symphysis. The addition of these gauges will help quantify the sacroiliac joint flexion during loading, and will help better define load distribution through the pelvis. The joint compliance coupled with the axial and rotational stiffness would be important for ATD development.

Finally, an acoustic sensor should be adhered to the sacrum to ensure accurate timing differences if the sacrum and other parts of the pelvis fail during a test. Additional sensors may help determine timing of distal fractures, and give additional response data for the complex geometry of the pelvis.

THESIS SUMMARY AND CONCLUSIONS

The primary focus of this research thesis was to investigate the failure tolerance of the component pelvis subjected to a high-rate vertical loading event, and calculate the axial stiffness. This thesis provides axial stiffness and response corridors up to failure. It also identifies two primary load paths through the pelvis, but cannot discern how the load is distributed between the two paths.

In this study, a test rig to accommodate the component pelvis, was built based on design principles from U.Va.'s whole body blast rig. The rig was constrained for Z-axis translation only and employed a six-axis load cell as well as accelerometers to quantify the boundary conditions prescribed to a test specimen. While the effective mass was an integral part of the test rig design, future testing may want to investigate whether having a non-fixed boundary on the superior side of the sacrum would be beneficial.

A total of 10 PMHS component pelvises were instrumented and tested once at the same input condition. In each test, there was a failure at the interface with the rigid potting medium. The average force at failure was calculated to be -5949 ± 1777 N and the average moment at

failure was 311 ± 157 Nm. They both occurred at 4 ± 0.6 ms. The force-deflection data revealed the pelvis had an axial stiffness of 995 ± 159 kN/m. The kinematic and moment response data both showed that the pelvis rotated in the positive direction about the y-axis. The distal pelvis fractures revealed two primary load paths, but the data collected cannot discern how the load was distributed between the sacrum and ischium.

These experimental results offer a first look at the response of the pelvis when subjected to high-rate vertical loading under the prescribed boundary conditions. Only the data up to failure should be considered reliable response data, but it can be used to help further develop ATDs or computer models used in blast loading conditions.

For future testing, additional loading rates and postures need to be explored in order to develop a more thorough understanding of the response of the pelvis. Isolating load paths should be considered in order to evaluate the effects on pelvis response when loaded only through the ischium or sacrum. The addition of more instrumentation will help quantify kinematic and deformation differences between the sacrum and the rest of the pelvis. Additionally, to minimize the likelihood of a failure at the pot, alternate potting techniques should be explored to hold on to the pelvis.

References

- Alvarez, John. 2011. *Epidemiology of Blast Injuries in Current Operations*. North Atlantic Treaty Organization Research and Technology Organization.
- Bailey, Ann M., John J. Christopher, Kyvory Henderson, Fred Brozoski, and Robert S. Salzar. 2013. "Comparison of Hybrid-III and PMHS Responses to Simulated Blast Loading Conditions." *IRCOBI Conference 2013*. Gothenburg, Sweden. 158-170.
- Bailey, MD, James R., Daniel J. Stinner, MD, Lorne H. Blackbourne, MD, Joseph R. Hsu, MD, and Michael T Mazurek, MD. 2011. "Combat-Related Pelvis Fractures in Nonsurvivors." *Journal of Trauma* 71 (1).
- Belmont, Jr., Philip J., Andrew J. Schoenfeld, and Gens Goodman. 2010. "Epidemiology of Combat Wounds in Operation Iraqi Freedom and Operation Enduring Freedom: Orthopaedic Burden of Disease." *Journal of Surgical Orthopaedic Advances, Volume 19 Number 1*.
- Bouquet, Robert, Michelle Ramet, Francois Bermond, Yves Caire, Youcef Talantikite, Stephan Robin, and Eric Voiglio. 1998. "Pelvis Human Response to Lateral Impact." *16th Enhanced Safety of Vehicles Conference*.
- Cesari, Dominique, and Michelle Ramet. 1982. "Pelvic Tolerance and Protection Criteria in Side Impact." *Proceeding of Stapp Car Crash Conference*. Society of Automotive Engineers. 145-154.
- Chamouard, F., F. Brun Cassan, J.Y. Le Coz, F. Guillon, and L. Bouchard. 1993. "Simulation of The Human Behavior in Lateral Impact." *International Research Council on Biomechanics of Injury*. 159-173.
- Clauser, Charles E., John T. McConville, and J. W. Young. 1969. *Weight, Volume, and Center of Mass of Segments of the Human Body*. National Technical Information Service.
- Crandall, J, S Kuppa, G Klopp, G Hall, W Pilkey, and S Hurwitz. 1998. "Injury mechanics and criteria for the human foot and ankle under axial impacts to the foot." *International Journal of Crashworthiness* 3 (2): 147-162.
- Dankaerts, Wim, Peter O'Sullivan, Angus Burnett, and Leon Straker. 2006. "Differences in Sitting Postures are Associated With Nonspecific Chronic Low Back Pain Disorders When Patients are Subclassified." *SPINE, Volume 31, Number 6* 698-704.
- Funk, J, J Crandall, L Turret, C MacMahon, C Bass, K Khaewpong, and R Eppinger. 2002. "The axial injury tolerance of the human foot/ankle complex and the effect of Achilles tension." *Journal of Biomechanical Engineering* 124: 750-757.
- Guillemot, H, C Got, B Besnault, F Lavaste, S Robin, JY Le Coz, and JP Lassau. 1998. *Pelvic Behavior in Side Impact Collisions: Static and Dynamic Tests on Isolated Pelvic Bones*. National Highway Transportation Safety Administration.
- Guillemot, H, C Got, B Besnault, J Y Le Coz, and JP Lassau. 1997. "Pelvic Injuries in Side Impact Collisions: A Field Accident Analysis and Dynamic Tests on Isolated Pelvic Bones." *Society of Automotive Engineers* 91-100.
- Guillemot, Herve, Wafa Skalli, Francois Lavaste, Claude Got, and Jean Yves Le Coz. 1995. "Static Behavior of the Pelvic Bone under Side Loading Conditions." *International Conference on Pelvic and Lower Extremity Injuries Proceedings*. The National Highway Traffic Safety Administration, U.S. Department of Transportation. 147-152.
- Lessley, D., J. Crandall, G. Shaw, R. Kent, and J. Funk. 2004. "A Normalization Technique for Developing Corridors from Individual Subject Responses." *SAE Technical Paper 2004-01-0288*.

- Lewis, Matthew E. 2006. "Survivability and Injuries from Use of Rocket-Assisted Ejection Seats: Analysis of 232 Cases." *Aviation, Space, and Environmental Medicine* 77 (9): 936-943.
- McKay, B, and C Bir. 2009. "Lower Extremity Injury Criteria for Evaluating Military Vehicle Occupant Injury in Underbelly Blast Events." *Stapp Car Crash Journal* 53: 229-249.
- Ramasamy, A, A Hill, S Masouros, J Gibb, A Bull, and J Clasper. 2010. "Blast-related Fracture Patterns: A Forensic Biomechanical Approach." *Journal of the Royal Society* 8: 689-698.
- Ramasamy, Arul, Spyros D. Masouros, Nicolas Newell, Adam M. Hill, William G. Proud, Katherine A. Brown, Anthony M. J. Bull, and Jon C. Clasper. 2011. "In-vehicle extremity injuries from improvised explosive devices: current and future foci." *Philosophical Transactions of The Royal Society B* (366): 160-170.
- Salzar, R. S., D. Genovese, C. R. Bass, J. R. Bolton, H. Guillemot, A. M. Damon, and J. R. Crandall. 2009. "Load path distribution within the pelvic structure under lateral loading." *International Journal of Crashworthiness* 1-12.
- Salzar, Robert S., Cameron R. "Dale" Bass, Richard Kent, Steve Millington, Martin Davis, Scott Lucas, Rodney Rudd, et al. 2006. "Development of Injury Criteria for Pelvic Fracture in Frontal Crashes." *Traffic Injury Prevention* 7: 299-305.
- Salzar, Robert S., James R. Bolton, Jeff R. Crandall, Glenn R. Paskoff, and Barry S. Shender. 2009. "Ejection Injury to the Spine in Small Aviators: Sled Tests of Manikins vs. Post Mortem Specimens." *Aviation, Space, and Environmental Medicine* 80 (7): 621-628.
- Schueler, F, R Mattern, F Zeidler, and D Scheunert. 1995. "Injuries of the Lower Legs - Foot, Ankle Join, Tibia; Mechanisms, Tolerance Limits, Injury-Criteria Evaluation of a Recent Biomechanics Experiment-Series." *Proceedings of IRCOBI Conference*. Brunnen, Switzerland. 33-45.
- Society of Automotive Engineers. 1995. *J211-1 Rev. March 1995*. SAE Safety Test Instrumentation Standards Committee.
- Stemper, B, N Yoganandan, J Baisden, F Pintar, and B Shender. 2012. "Rate-Dependent Failure Characteristics of Thoraco-Lumbar Vertebrae: Application to the Military Environment." *ASME 2012 Summer Bioengineering Conference*. 1283-1284.
- Wang, J, R Bird, B Swinton, and A Krstic. 2001. "Protection of Lower Limbs Against Floor Impact in Army Vehicles Experiencing Landmine Explosion." *Journal of Battlefield Technology* 4 (3).
- Wu, Ge. 2002. "Letter to the editor." *Journal of Biomechanics* 35: 543-548.
- Yoganandan, N, F Pintar, S Kumaresan, and M Boynton. 1997. "Axial impact biomechanics of the human foot-ankle complex." *Journal of Biomechanical Engineering* 119 (4): 433-437.

APPENDIX A: 'A' and 'C' strain gauge data from rosette strain gauges.

Pelvis 002

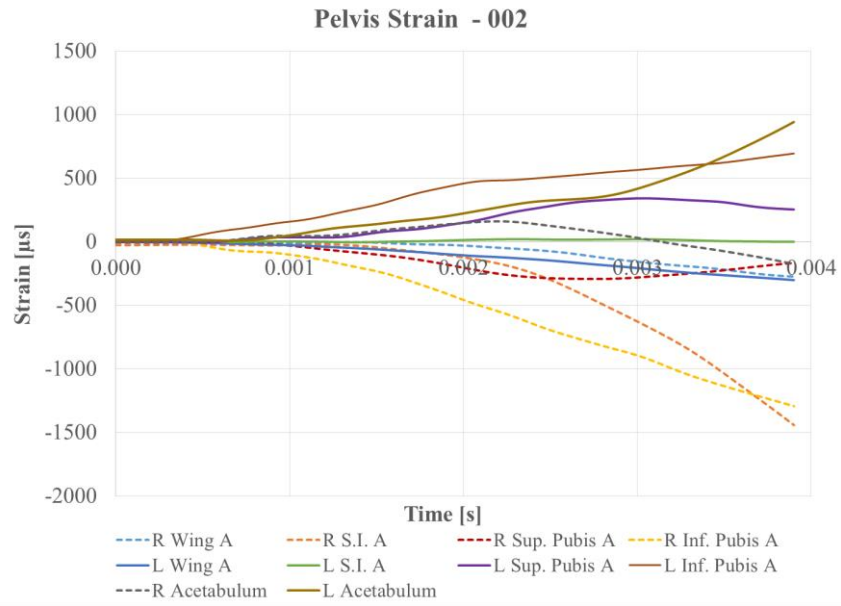


Figure A-1: Strain gauge data from the 'A' gauges for test 002.

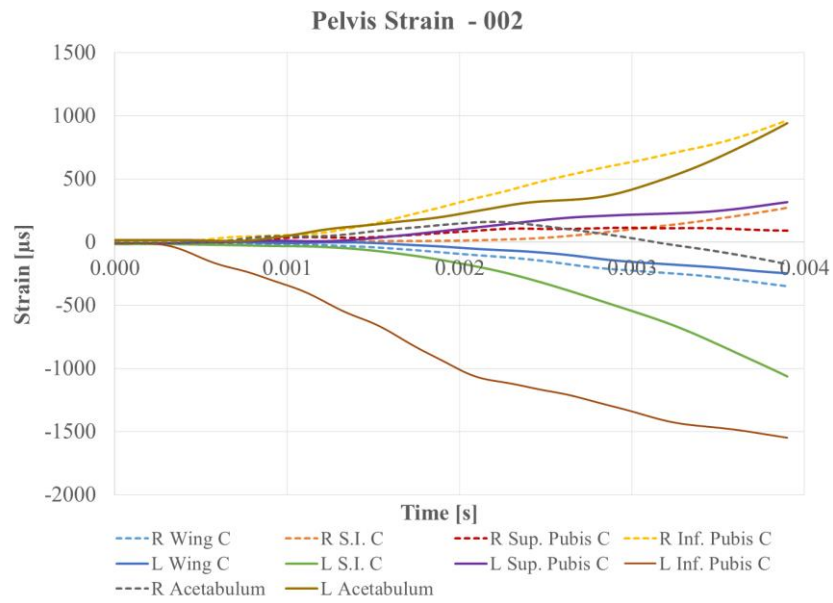


Figure A-2: Strain gauge data from the 'C' gauges for test 002.

Pelvis 003

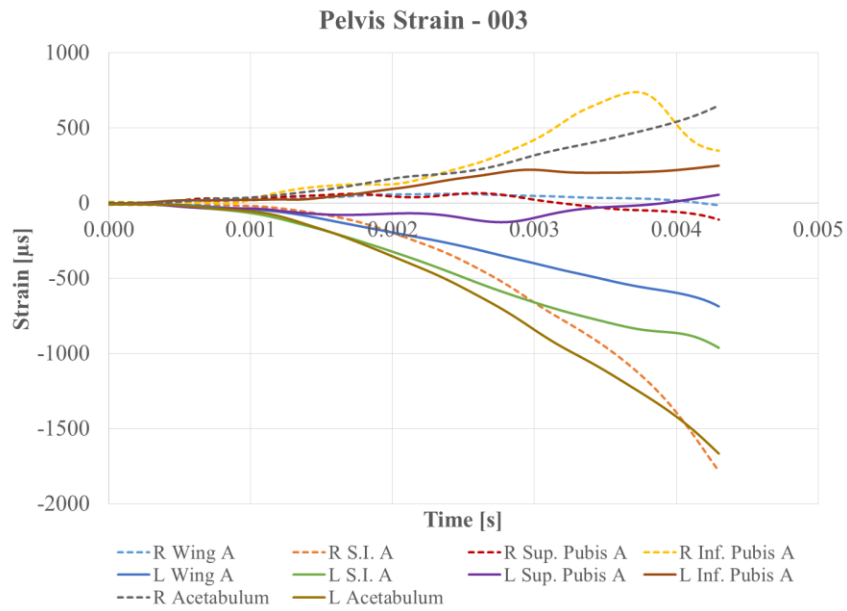


Figure A-3: Strain gauge data from the 'A' gauges for test 003.

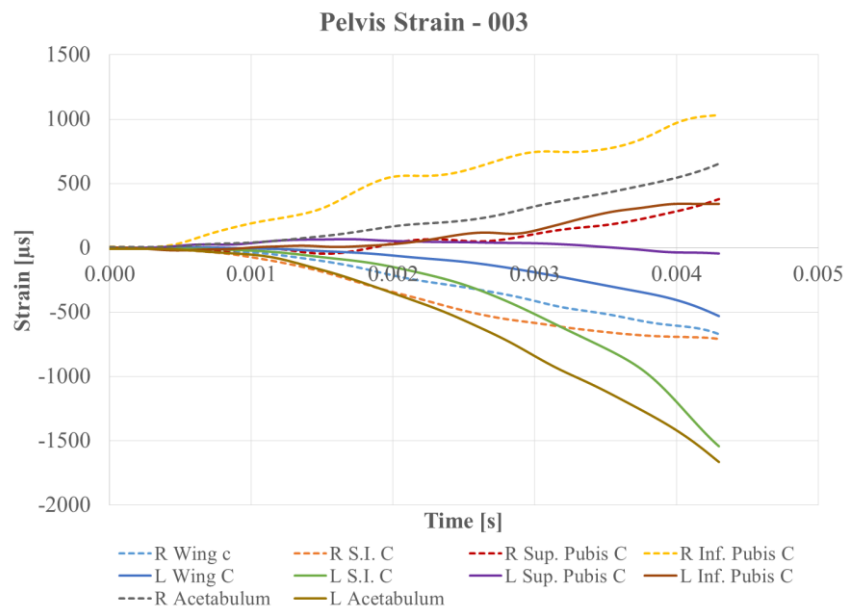


Figure A-4: Strain gauge data from the 'C' gauges for test 003.

Pelvis 004

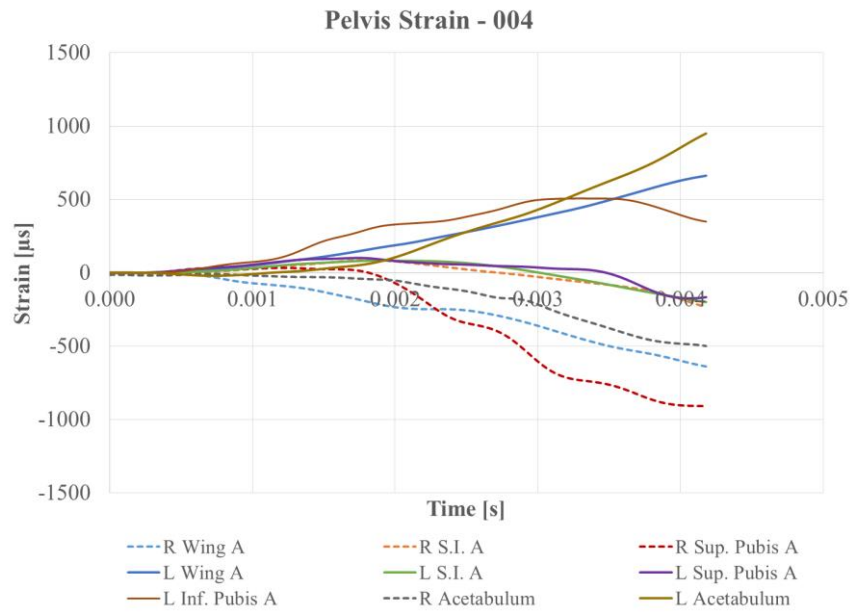


Figure A-5: Strain gauge data from the 'A' gauges for test 004.

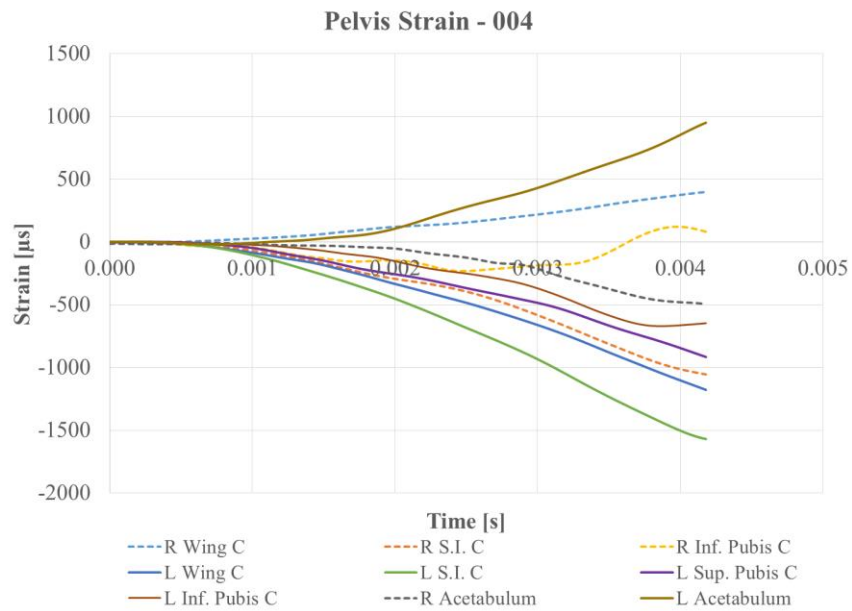


Figure A-6: Strain gauge data from the 'C' gauges for test 004.

Pelvis 005

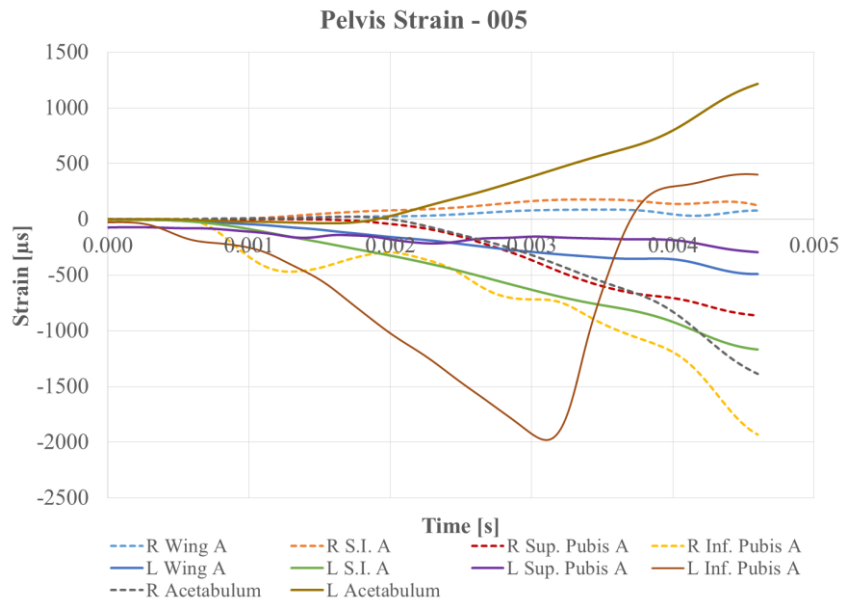


Figure A-7: Strain gauge data from the 'A' gauges for test 005.

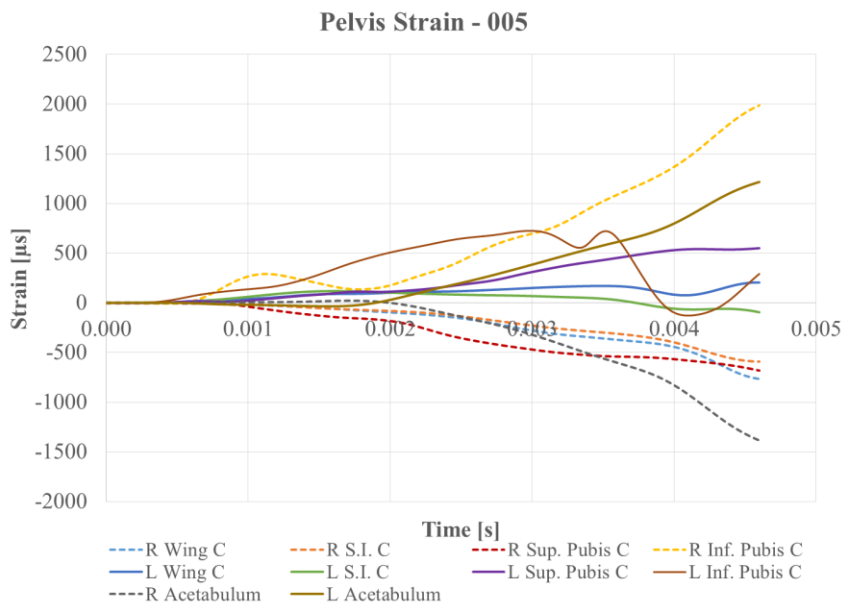


Figure A-8: Strain gauge data from the 'C' gauges for test 005.

Pelvis 006

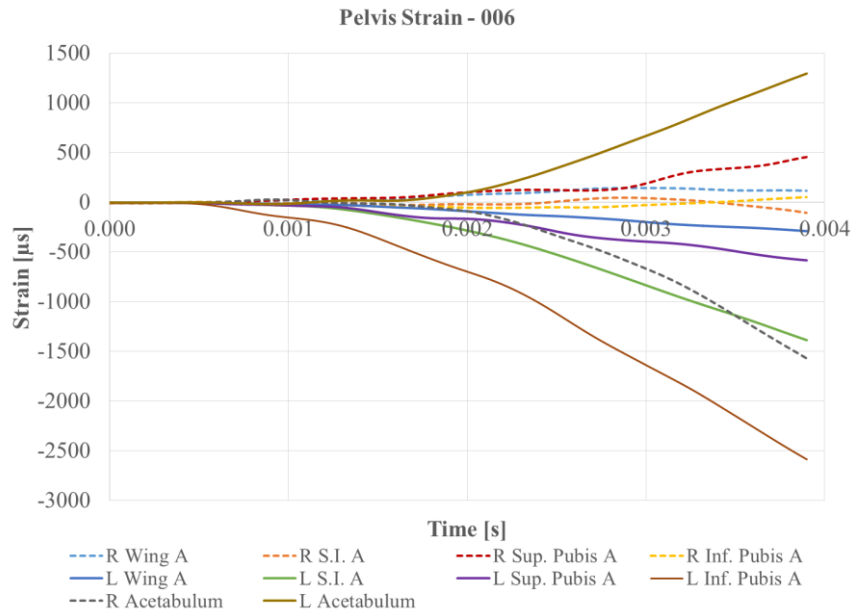


Figure A-9: Strain gauge data from the 'A' gauges for test 006.

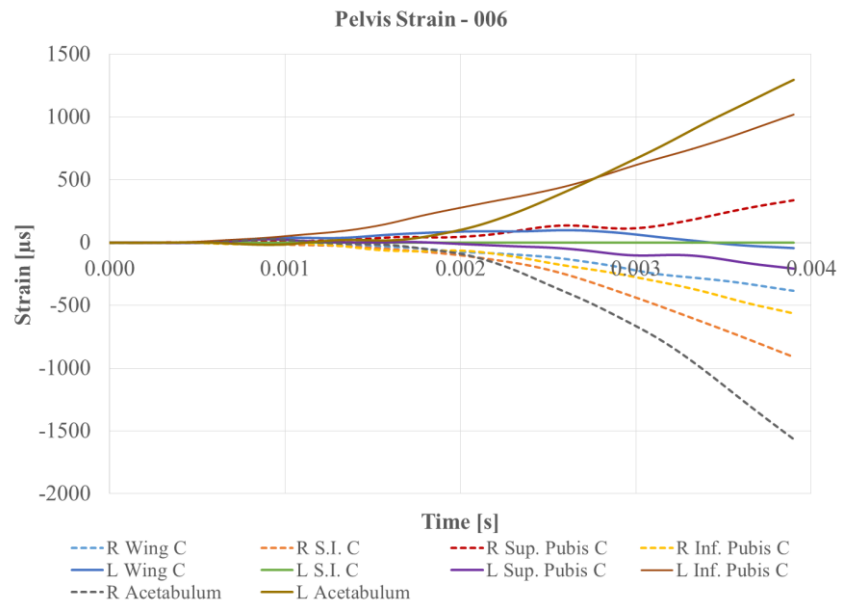


Figure A-10: Strain gauge data from the 'C' gauges for test 006.

Pelvis 007

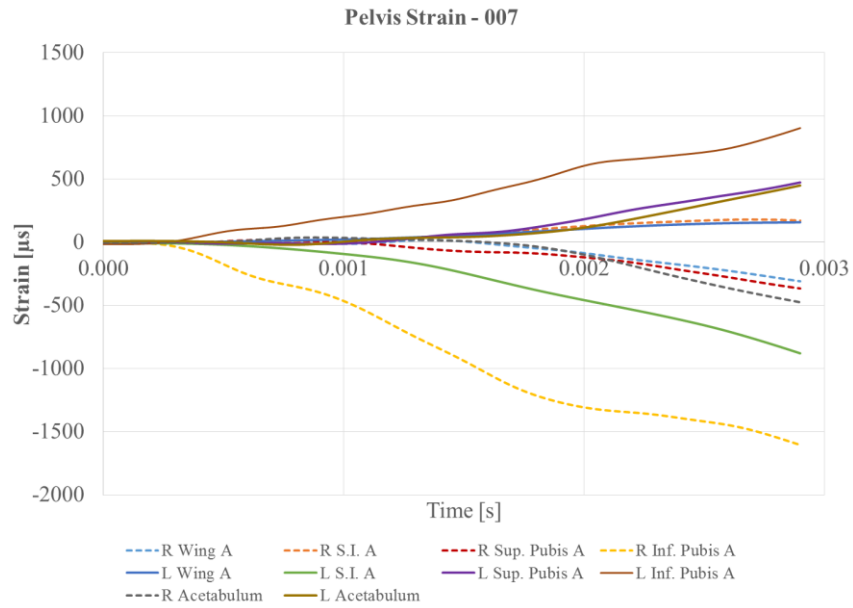


Figure A-11: Strain gauge data from the 'A' gauges for test 007.

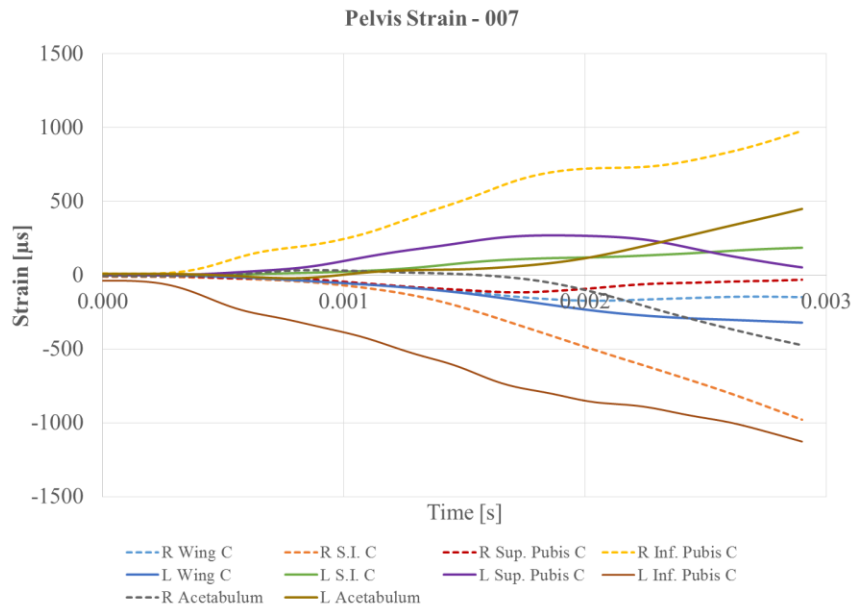


Figure A-12: Strain gauge data from the 'C' gauges for test 007.

Pelvis 008

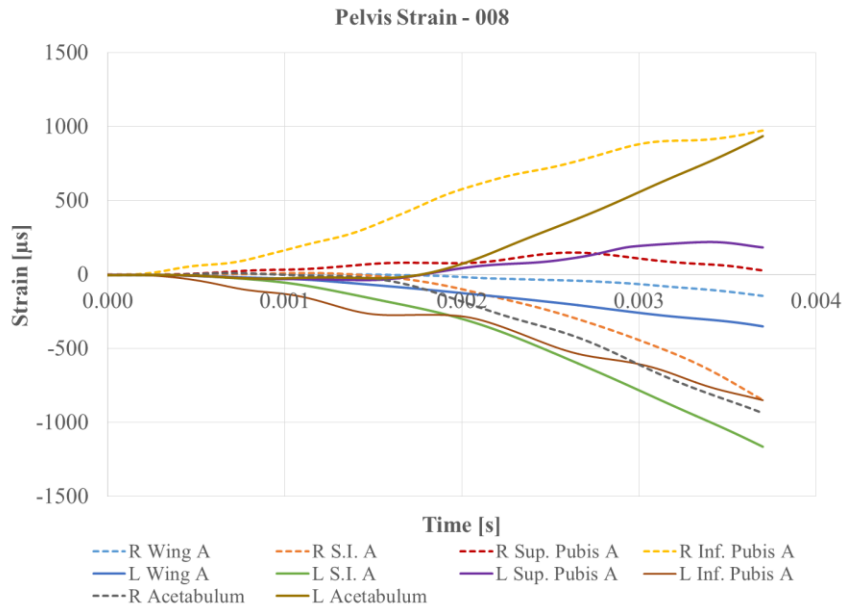


Figure A-13: Strain gauge data from the 'A' gauges for test 008.

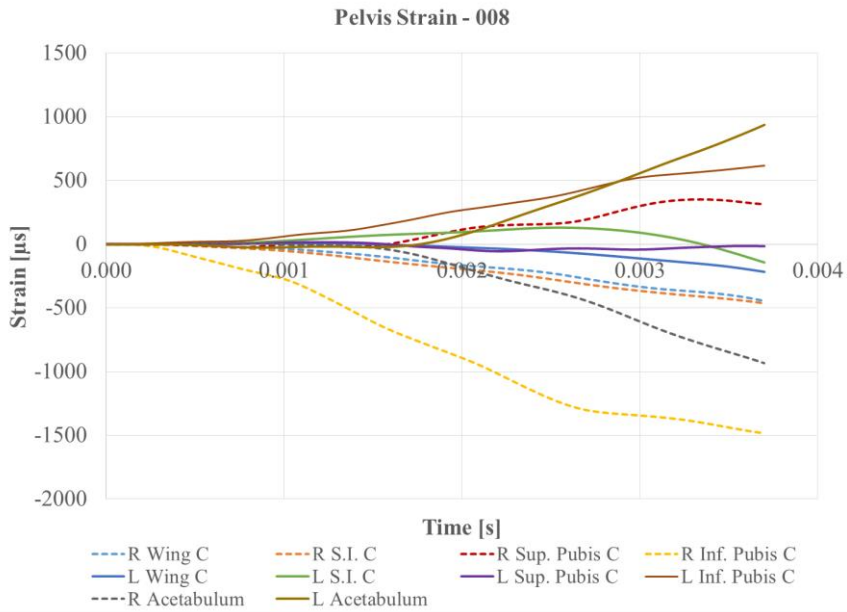


Figure A-14: Strain gauge data from the 'C' gauges for test 008.

Pelvis 009

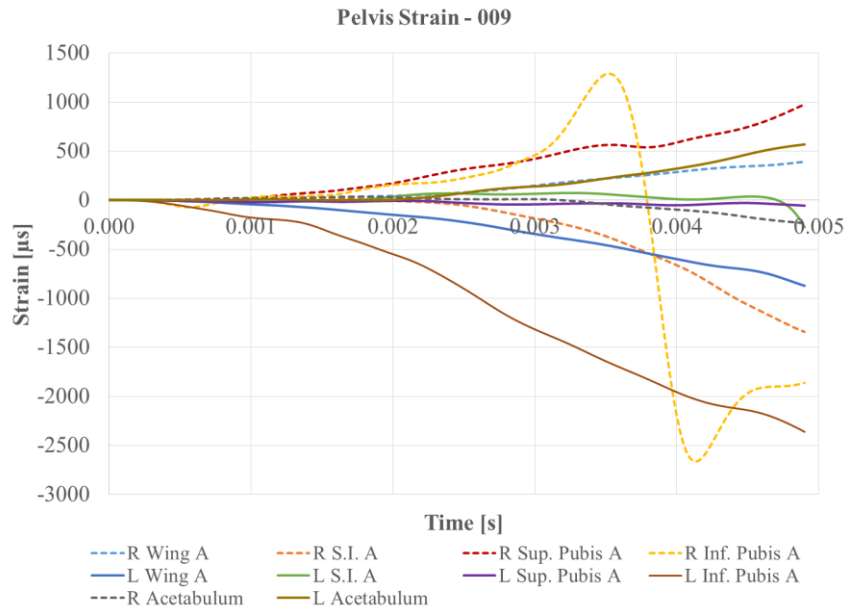


Figure A-15: Strain gauge data from the 'A' gauges for test 009.

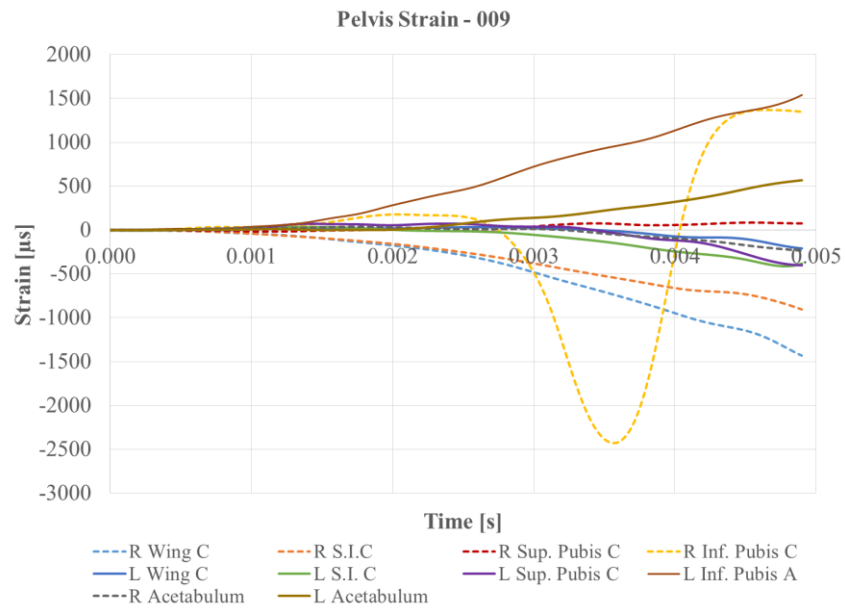


Figure A-16: Strain gauge data from the 'C' gauges for test 009.

Pelvis 010

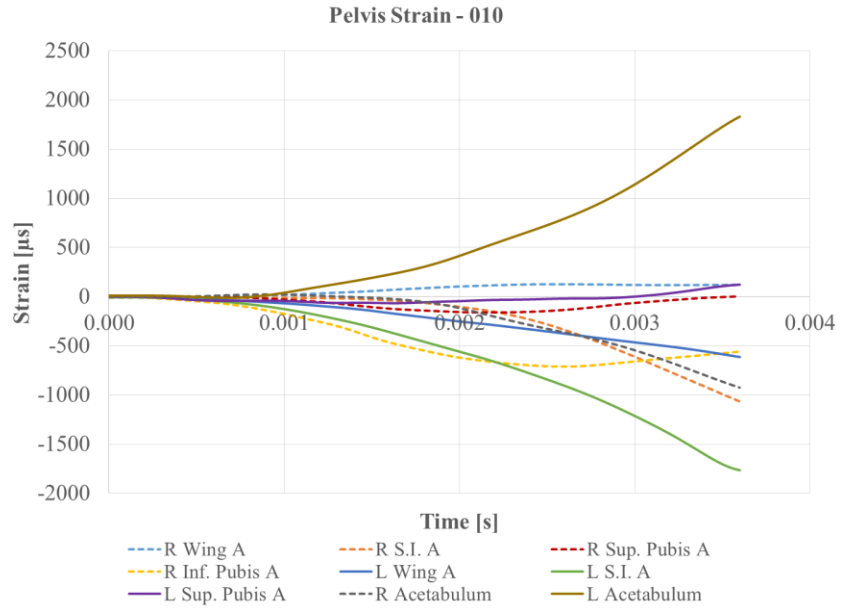


Figure A-17: Strain gauge data from the 'A' gauges for test 010.

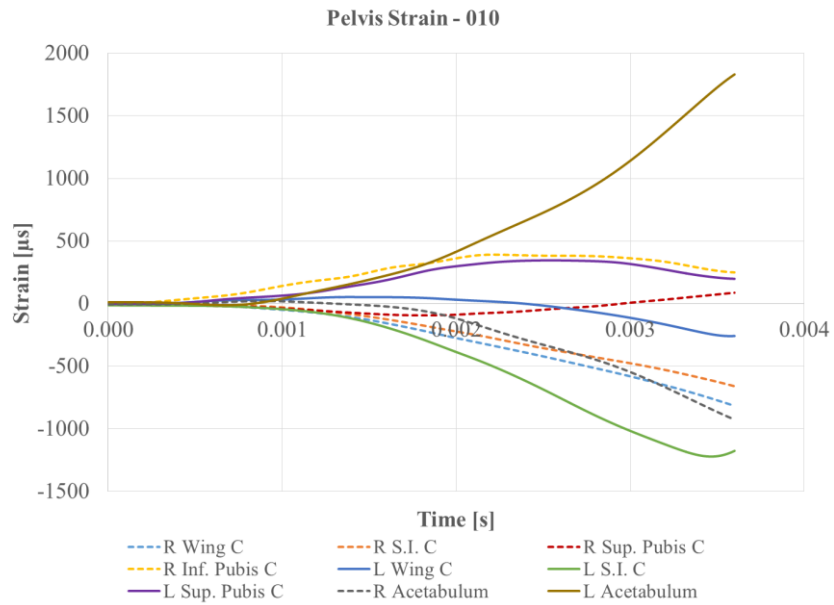


Figure A-18: Strain gauge data from the 'C' gauges for test 010.